

FEM ANALYSIS OF MASS TRANSFER THROUGH NON - SPHERICAL BUBBLES IN COPPER CONVERTER

A Thesis Submitted
in Partial Fulfilment of the Requirements
for the Degree of
MASTER OF TECHNOLOGY

by

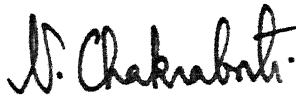
P. S. MOHANTY

to the

**DEPARTMENT OF METALLURGICAL ENGINEERING
INDIAN INSTITUTE OF TECHNOLOGY KANPUR
MARCH, 1990**

CERTIFICATE

Certified that this thesis work " FEM ANALYSIS OF MASS TRANSFER THROUGH NON-SPHERICAL BUBBLE IN MATTE COPPER CONVERTER" submitted by P. S. MOHANTY in partial fulfillment for the award of the degree of Master of Technology Indian Institute of Technology, Kanpur is a record of bonafide research work carried by him under our supervision and guidance. The work embodied in this thesis has not been submitted elsewhere for a degree or diploma.



N. CHAKRABORTI

Assistant professor

Dept. of Metallurgical Engg.

I. I. T. Kanpur.



T. SUNDARAJAN

Assistant professor

Dept. of Mechanical

I. I. T. Kanpur.

ME-1990-M-MOH-FEM

-8 OCT 1990

CENTRAL LIBRARY

Acc. No. 109077

C O N T E N T S

	page
List of figures	
Synopsis	i
<i>Chapter</i>	
1 INTRODUCTION	1
1.1. Copper Conversion	1
1.1a. Slag Forming	1
1.1b. Copper Making	2
1.2 Formation and Motion of Bubbles in Submerged Blown System	2
1.3 Dispersed Bubble Systems	5
1.4 Literature Review	6
1.5 Scope of the Present Study	13
2 MODEL FORMULATION	15
2.1 Assumptions in the Model	17
2.2 Governing Equations and Boundary Conditions	20
3 SOLUTION PROCEDURE	29
3.1 FEM Analysis	29
3.2 Types of Formulation	30
3.3 Derivation of Finite Element Equation	32
4 RESULT AND DISCUSSION	46
4.1 Validation of the Model for Shape Calculations	46
4.2 Results and Discussions	47
5 CONCLUSION AND SUGGESTIONS FOR FUTURE WORK	51
<i>Appendix</i>	
1 THE MEAN CURVATURE OF A SURFACE OBTAINED BY REVOLUTION OF A CURVE ABOUT AN AXIS	52
2 COUPLING OF ENERGY EQUATION WITH MOMENTUM EQUATION	56
3 CONDITION AT INFINITY OF OSEEN TYPE	57
4 FRONTAL METHOD	59
5 TRANSFINITE INTERPOLATION	61

ACKNOWLEDGEMENTS

It is with great apprehension that I have taken up the task of expressing my deep sense of gratitude to my guides Dr. Sundararajan and Dr. N. Chakraborti. This is because of the fact that mere words will prove to be insufficient in conveying the help and guidance extended by them. Each stage of my thesis was closely monitored by them. Their suggestion and words of encouragement went a long way in making this work a success. Knowing fully well the limitations the language has imposed on me, I would like to convey my sincere thanks for their invaluable guidance.

I also acknowledge the assistance rendered by my friends and faculties. I express my sincere thanks to all those who

SYNOPSIS

In the present work, buoyancy-driven motion of deformable bubble through a liquid metal bath during conversion has been studied. The solution involves viscous past deformable bubbles. The effect of volume of the bubble, its position in the bath, on the shape has been investigated. shape of the bubble and the flow around it is dealt in a cou manner. During different stages of copper making the reac species are transported to the bubble-liquid interface. unsteady transport of the species and its distribution around bubble has been studied. Since no suitable reaction constant available in literature at this stage, it is assumed that reaction is mass transfer controlled.

The analysis involves solution of Navier-Stokes equations, Continuity equation, Laplace equation and diffusion equations. This also involves certain relationships concerning differential geometry of surface of revolution.

For handling such moving boundary problems, Finite Element Method has been used. During the solution each time geometry changes, and hence, the problem calls for an automatic mesh generation and coordinate fixing. For this purpose transfinite interpolation is used.

Since much experimental information is not available, such a system to check the validity of the formulation and calculation schemes, prediction of a rain drop shape has been compared with experimental photograph which matched to a very high degree. Some limiting deformations have been considered. This is because of the formidable difficulties encountered in solving the Navier-Stokes equations for flow around highly distorted bubbles.

CHAPTER I

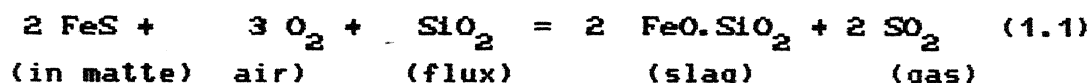
INTRODUCTION

Bubbles play a key role in many natural phenomena and in a host of industrial applications. Reacting gas bubbles are of fundamental importance in many chemical and metallurgical operations such as absorption, floatation, degassing, steel making and copper conversion etc. There is relative motion between the bubbles and the surrounding fluid in all these cases. Consequently, the phenomenon of interest is the transfer of heat or species from one side of the bubble interface to the other. In the present study the interaction of bubbles in liquid matte in a copper converter is dealt with. The hydrodynamics of bubble motion and its bearing upon the rate of oxygen depletion from one bubble are highlighted.

1.1 Copper Conversion

The copper converting operation is carried out in a horizontal basic refractory lined Pierce-Smith type side blown converter. The matte that is charged into the converter consists of FeS and Cu₂S. Converting operation removes the iron and sulfur from the matte and results in the production of a crude blister copper. The converting operation consists of two stages namely:

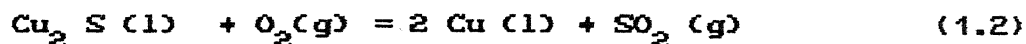
(a) Slag forming : This is the stage in which FeS elimination occurs. The probable reaction is



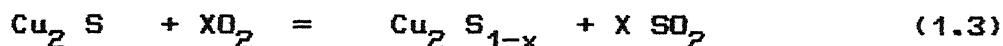
In this stage FeS is oxidized to FeO and Fe₃O₄ and sulphur is removed as SO₂. Silica flux is added for combining with FeO (and partly with Fe₃O₄) for slag formation. From thermodynamic considerations it can be shown that this stage ceases when the

matte contains less than 1% FeS. Liquid fayalite slag becomes saturated with magnetite and the principal product of the slag forming stage is the "White Metal" or impure liquid Cu_2S . The remaining sulfur is oxidized to SO_2 during copper making stage. At the end of the slag forming stage, the converter contains molten slag or fayalite ($2\text{FeO} \cdot \text{SiO}_2$) with 10-20 % solid magnetite(saturated) and up to 15 % dissolved and entrained copper and molten matte which is principally Cu_2S , with less than 1.5% FeS [76Bis]. These two phases are immiscible with the slag floating on top of the matte.

(b) Copper making: Metallic copper is formed by the following reaction.



Initially, when air is blown through Cu_2S , sulphur is removed as SO_2 to give a sulphur- deficient white metal. No metallic copper is formed during this stage. The overall reaction is as follows:



Subsequent blowing of air causes the appearance of a second liquid phase of blister copper containing 1-2 % S. The metallic blister copper phase is more dense than sulphur deficient Cu_2S phase and sinks to the bottom. Further blowing of air results in additional sulphur being removed from the system. Eventually the system becomes so sulphur deficient that the sulphide phase disappears and only blister copper remains. The final sulphur is removed by further blowing and the converting process is carried out till a trace of Cu_2O appears.

1.2 Formation and motion of bubbles in submerged blown system:

Considerable amount of both theoretical and experimental literature is available regarding the formation of bubbles from submerged nozzles. Indeed, this has become a separate field of study. When liquid does not wet the nozzle, the bubbles tend to form at the outer circumference of the nozzle. They grow

up to a critical size and then get detached from the nozzle. The critical [79Sze] size is given by the relation:

$$d_{B, d} = \left[\frac{\sigma d_{n,0}}{\rho_l (\rho_l - \rho_g)} \right]^{1/2} \quad (1.4)$$

where $d_{n,0}$ is the outside diameter of the nozzle

The turbulence established during the blow helps in detaching the bubbles. In metallic systems a higher surface tension prevails at the gas-liquid interface which tends to prevent the break up of bubble thus large size bubbles are formed in such situations.

After getting detached from the tip of tuyuers, the bubbles rise towards the free surface due to buoyancy. During the rise the large bubbles often get fragmented into smaller bubbles and due to buoyancy they rise up. The velocity with which the bubbles rise through the liquid is principally determined by the buoyancy force that drives the bubble upwards and the viscous and form drags which retard the bubble motion. When these counter-acting forces balance each other the bubble rises with a steady velocity. The important fact associated with the motion are:

- (a) The bubble is not rigid and thus the forces acting on it may deform its shape.
- (b) The gas contained in the bubble under goes circulation which in turn would affect the drag force.
- (c) The volume of the bubble increases as the bubble rises towards the free surface. This, in turn, influences the drag phenomena and the bubble velocity.

The above mentioned factors affect the system drastically. The deformation becomes severe in a high density system like metallic bath and consequently influences the flow field and transport of species and heat to a large extent. The flow in general, can be characterized by the dimensionless groups of Reynolds number, Weber number, Eötvös number and Morton number. The deformation phenomena and their dependence on the

characteristic numbers will be discussed in more detail in latter chapters, as these form major objectives of the present study. The drag force affects the motion of the bubble to a large extent. The total drag coefficient for solely moving solid spheres given by the expression

$$C_{DSt} = 24 / Re \quad (1.5)$$

according to Stokes law. Two third of this drag arises from skin friction and one third is due to form drag. The corresponding terminal velocity is given as: [78C1i]

$$U_{TS} = \frac{2}{9} \frac{g d^2 (\rho_s - \rho_f)}{18 \mu} \quad (1.6)$$

The Hardmard-Rybczynski [78C1i] theory predicts that the terminal velocity of a spherical bubble should be about 50 % higher than that of a rigid sphere of same size and density. However it is commonly observed that small bubbles and drops tend to obey Stokes law rather than the corresponding Hardmard-Rybczynski results. Moreover, internal circulation is essentially absent. Three different mechanisms have been proposed for this phenomenon.

Bond and Newton [78C1i] found that small bubbles and drops followed Stoke's law while, with increasing diameter, there was a rather sharp increase in velocity towards the Hardmard-Rybczynski value. they suggested that a circulating particle requires energy locally to stretch on inter-facial area element over the leading hemisphere, which subsequently shrinks over the rear hemisphere. It was hypothesized that this process caused additional tangential stresses to retard the particle.

Boussinesq [78C1i] proposed that lack of internal circulation in bubbles and drops is due to an inter-facial mono-layer which acts as viscous membrane. A constitutive equation involving the two parameters of surface shear viscosity and surface dilational viscosity was proposed for the interface, in addition to the surface tension.

The most reasonable explanation for the absence of internal circulation for small bubbles and drops was provided by Frumkin and Levich [78C11]. Surface active substances tend to accumulate at the interface between two fluids, thereby reducing the surface tension. When a drop or bubble moves through a continuous medium, it adsorbs surface active materials at the interface. The adsorbed particles are swept to the rear leaving the frontal region relatively less contaminated. The resulting concentration gradient leads to a tangential gradient of surface tension which in turn causes a tangential stress, tending to retard surface motion.

1. 3. Dispersed Bubble Systems:

Isolated bubbles behave in quite a different manner from a dispersed system of bubbles. In the case of an array of bubbles, each bubble will be affected by the influence of its neighbors. The behavior of such systems is quite complex and not well understood. Most of the experimental measurements are restricted to the water-air system and that too essentially at room temperature. Extrapolation of such findings to a high temperature metallic system is highly impracticable.

Dispersed bubble systems are usually formed by the injection of a gas stream into a liquid through one or multiple orifices. In some cases however bubbles are formed through heterogeneous nucleation. The principal parameters used for the characterization of the multiple bubble systems are the superficial velocity, the mean velocity, the void fraction or gas hold up, the surface area per unit volume and the mean bubble diameter.

$$U_{BS} = \frac{\text{vol. flow rate of gas}}{\text{cross sectional area of vessel}}$$

and

$$\epsilon_g = \frac{\text{Vol. of gas bubbles}}{\text{Vol. of gas and liquids.}}$$

where U_{BS} = superficial velocity,

ϵ_g = void fraction.

Dispersed bubble systems may be divided somewhat arbitrarily as:-(i) Bubbling Systems ($\epsilon_g < 0.3$), (ii) Froths ($\epsilon_g = 0.4 - 0.6$), and (iii) Foams ($\epsilon_g = 0.9 - 0.98$). Among metal processing systems with argon stirred ladles, the gaseous deoxidation of copper and copper converting system will fall into category (i) i.e. the bubbling systems.

1. 4. Literature Review:-

Most of the experimental and theoretical studies of bubble formation and chemical reaction at the bubble-liquid interface have appeared in chemical engineering and fluid mechanics literature. Many of these studies have been concerned with aqueous and organic liquids. The simple theoretical model of Davidson and co-workers was found to describe bubble formation in mercury at room temperatures [81Ash]. However when applied to industrial converters the model predicts a bubble frequency 2 to 3 times lower than that measured. Since Davidson model can only be correctly applied to a stagnant, isothermal and non-reactive system, this discrepancy is not surprising.

Ashman and Co-workers [81Ash] studied bubble formation in a copper converter. According to them, bubbles that form at tuyers of a copper converter are large and their size is strongly dependant on the volume rate of air flow, heat transfer and bath circulation velocity. One important aspect of these findings is that the bubbles occupy a significant fraction of the liquid space between the tuyers and the bath surface. About 40 % of oxygen is consumed during bubble formation at the tuyers and the rest reacts during rise and break-up of the bubble.

Most of the experimental as well as the theoretical results available are for the water-air system and these have been usually represented in terms of the following dimensionless groups.

Reynolds Number,
$$R = \frac{\rho d_e U}{\mu} \quad (1.7)$$

$$\text{Eötvös Number, } E = \frac{g d_e^2 \rho}{\sigma} \quad (1.8)$$

$$\text{Morton Number, } M = \frac{g \mu^4}{\rho \sigma^3} \quad (1.9)$$

The commonly used drag co-efficient (C_D) and Weber number are not independent of this set, since

$$C_D = \frac{4 g d}{3 U^2} = \frac{4 E^{3/2}}{3 R^2 M^{1/2}} \quad (1.10)$$

$$W = \frac{\rho U^2 d_e}{\sigma} = \frac{R^2 M^{1/2}}{E^{1/2}} \quad (1.11)$$

In the above equations, the characteristic length $d_e = (6V/\pi)^{1/2}$ is the volume equivalent diameter of a bubble of volume V and U is its terminal rise; ρ , μ and σ are respectively, the density viscosity and surface tension of the liquid and g is the acceleration due to gravity. Fig-1.1, gives a pictorial summary of the shapes of the bubbles in different regimes of these non-dimensional groups.

Till date, the number of theoretical papers dealing with ideal flow about bubbles is large and the viscous flow past deformable bubbles has seldom been investigated. This is connected with the formidable difficulties that are encountered in solving the Navier-Stokes equations with deformable free boundary. The class of problems with a deformable boundary is characterized by the existence of one or more boundaries of the flow domain whose shape is dependent upon the viscous and pressure forces generated by the fluid motion. In this case the shape of the boundary and the form of the velocity and pressure fields in the fluid are intimately connected and one must solve for the boundary shape as a part of the overall solution of a particular problem. The most common problems of this type in fluid mechanics occur in the motion of two immiscible fluids which are contiguous

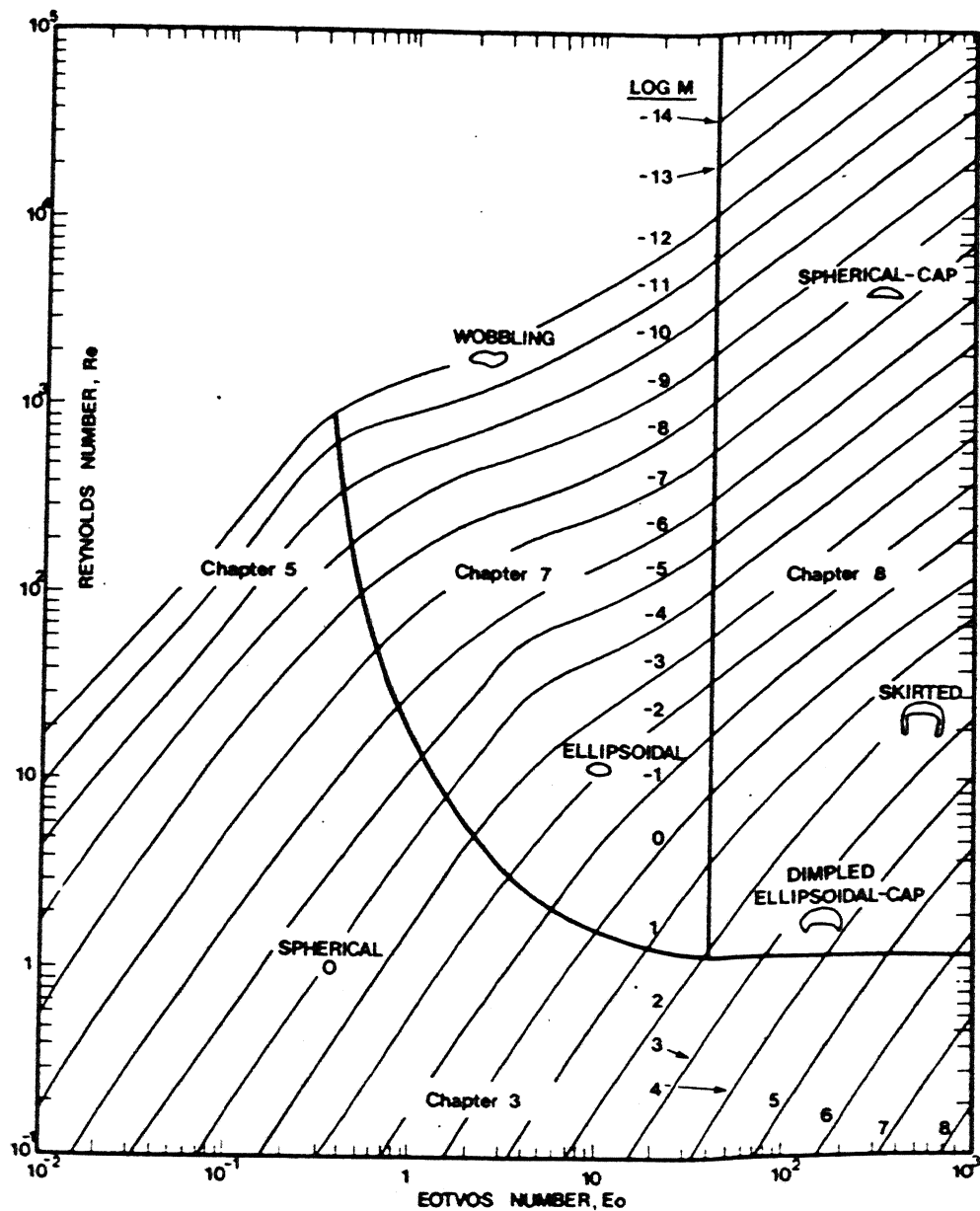


Fig. 1.1. Shape Regimes for Bubbles and Drops in Unhindered Gravitational Motion through Liquids.

with a common interface e. g. gas-liquid interface. For this reason a number of limiting cases have been treated theoretically either at low or very high Reynolds numbers in various combinations with or without deformability of the interface; but no satisfactory theory exists as yet, except for the cases of very small deformations.

The existing published literature on free boundary problems in fluid mechanics is quite extensive in number, but limited in scope. Three distinct solution methods can be identified. By far the majority of papers are concerned with asymptotic solutions or limiting solutions in which the interface shape while unknown, deviates only slightly from some predefined configuration. In the case of bubble motion, a number of authors have used the so called "domain perturbation" method to solve for the first deviation from a spherical bubble in a variety of flows [34Tay], [64Acr]. Levich solved the problem of boundary layer flow past Spherical non-deformable bubbles at very high Reynolds number and very low Weber number [59Lev]. Moore acknowledged to some extent the deformation of bubble surface, considering the boundary layer around an elliptic gas bubble [65Moo]. Elswawi extended Moore's analysis and accounted for the interaction between boundary layer and the shape of bubble [74Els]. In addition a similar approach has been used to consider the first deviation from the limiting form of a slender body with an arbitrarily small radius-to-length ratio, which is relevant for example, to low viscosity drops in uniaxial extensional flows with a sufficiently high strain rate [64 Tay] and [78 Acr].

A second method of solution suitable for free boundary problems is the boundary integral technique which is restricted to limiting cases of either zero or very high Reynolds number, where the governing differential equation reduces to Laplace's equation. In this method, fundamental solutions of the linear governing equations are used to reduce the general n -dimensional problems to the solution of $(n-1)$ -dimensional integral equations. The boundary integral method is not restricted to small deformations. Indeed solutions have been obtained which exhibit large departures from predefined shapes [76You], [81Mik], [82Lee]. In the analysis

done by Miksis, Vanden-Broeck and Keller, they have considered very high Reynolds number flow. The effect of viscosity are confined to a thin boundary layer around the bubble. Then, by treating the surrounding fluid to be incompressible, the motion can be represented as potential flow which automatically satisfies the Navier-Stokes equation. One way to complete the formulation is to match this potential flow to the flow in the boundary layer. But it is difficult to do so because even for a spherical bubble the flow in the boundary layer is not known near the rear stagnation point on the axis of symmetry at $\theta = \pi$. As an alternative they have assumed the potential flow right up to the boundary which yields an exact solution of the Navier-Stokes equations throughout the fluid, with vanishing normal velocity on the surface of the bubble. However the restriction to potential flow reduces the usefulness of the study and for non-spherical bubble the potential flow assumption is not appropriate.

The third and most important class of free-boundary problems, which are not restricted to any limiting cases has been studied recently. Ryskin and Leal used finite difference method which incorporates a numerically generated orthogonal co-ordinate system, which is "boundary-fitted" in the sense that all the boundary surfaces of the solution domain (including the free boundary whose shape is determined as a part of the solution) coincides with a co-ordinate line (or surface) of the co-ordinate system [84Rys]. Thus the problem of interpolation between nodal points of the finite difference grid when the latter is not coincident with the physical boundaries is avoided altogether. Indeed, the existence of the interpolation problem in the first place seems to be a consequence of the common analytically generated co-ordinate systems, such as cylindrical and spherical systems, when the latter do not correspond to the natural boundaries of the solution domain. The mapping procedure was restricted to two dimensional and axisymmetric flow domains. The boundary fitted co-ordinate system is denoted as (ξ, η, ϕ) with ϕ symmetry. In view of the assumed axisymmetry, these boundary fitted coordinates can be connected with the common cylindrical coordinates (x, r, ϕ) via a pair of mapping functions $x(\xi, \eta)$ and

$\sigma(\xi, \eta)$ which satisfy the Laplace equations in covariant form:

$$\frac{\partial}{\partial \xi} \left[f \frac{\partial \sigma}{\partial \xi} \right] + \frac{\partial}{\partial \eta} \left[\frac{1}{f} \frac{\partial \sigma}{\partial \eta} \right] = 0 \quad (1.12)$$

$$\frac{\partial}{\partial \xi} \left[f \frac{\partial \sigma}{\partial \xi} \right] + \frac{\partial}{\partial \eta} \left[\frac{1}{f} \frac{\partial \sigma}{\partial \eta} \right] = 0 \quad (1.13)$$

where $f(\xi, \eta)$ is called the distortion function

With a similar approach Christov and Volkov [85Chr], considered viscous flow in intermediate Reynolds number and for relatively low Weber number. The problem of the moving boundary is tackled by means of an appropriate coordinate transformation. They considered a form of coupled boundary value problem for estimating the stream function, vorticity function and the shape of the bubble. The unknown shape which is defined as $r = R(\theta)$ poses considerable difficulties for which they introduced the transformation of independent variables by the expressions $r = \eta R(\theta)$, $\theta = \theta$. Thus the problem was transformed to a simple computational domain for solution purposes.

Though recently the steady rise of bubbles in viscous liquids has been intensively studied both theoretically and experimentally, the knowledge gathered about the shape of bubbles and patterns of the flow is still not complete. Experimental studies devoted to the motion of deformable drops or bubbles have been chiefly concerned with the estimation of the terminal velocity of rise. Only recently, some quantitative information concerning the shape of bubbles and the streamlines of flow around them, has been experimentally collected by Bhaga and Weber [80Bha]. They have presented experimental data in the form correlations for bubble rise velocity and shape. The basic techniques consist of photographing a rising bubble with a cine camera moving upwards at the same speed as the bubble. The rate of ascent of the camera could be varied. The camera elevator speed was set equal to the subject bubble speed from earlier calibration runs. Using this technique the bubble remained in the center of the frames in the cine film throughout its rise. The velocity

field around the rising bubble was visualized by hydrogen bubbles introduced electrolytically into the liquid. The liquid used was aqueous sugar solution with differing concentrations.

But much information is not yet reported about the shape of bubble and nature of flow in a liquid metal bath. There are evidences that bubbles in liquid metal show the behavior expected from more concentrated liquids. Because of large surface tension forces for liquid metals, the Morton number tends to be low. However metallic systems are prone to contaminations by surface active impurities which in turn, alter the bubble shapes drastically. The picture of two dimensional bubble in liquid mercury has been presented in fig-1.2 [78C1i]. For experimental convenience the bubble studies have usually dealt with rather large bubbles and , there is only limited data available for spherical or slightly deformed ellipsoidal bubbles in liquid metals. These data tend to suffer from abnormally high scatter due to experimental difficulties associated with opaque media and high temperature. Moreover, the cold model experiments are not solely concerned with steady rise, since during motion the bubble passes to regimes of lower pressure and hence the bubble volume increases. This is quite significant in molten metal baths of high density. The expansion would of course be greater if the melt is at a reduced pressure, as in the case of a vacuum degassing system.

Theoretical studies regarding spherical cap bubbles are still many. The well known analysis of the "spherical cap" bubble due to Davis and Tayler [50Dav] relates the speed of rise to the radius of curvature of the bubble at front stagnation point [66 Col], but the overall spherical cap shape is assumed a priori, rather than being determined as apart of full solution. According to Collins a gas bubble in liquid is termed large if the Reynolds number and Weber number associated with its motion are sufficiently high so that viscous and surface tension forces are insignificant compared with the inertial and gravity forces in determining its shape and velocity. The bubble then adopts the characteristics of spherical cap form discussed by numerous authors. In his theoretical study, Collins used a formerly



Fig. 1.2. Two-dimensional Nitrogen Bubble in Liquid Mercury.

developed equation which relates the bubble velocity U and the apparent curvature \bar{a} of the spherical cap, in the form :

$$U = 2/3 (g \bar{a})^{1/2} \quad (1.14)$$

Richardson and Bradshaw as quoted in [67Rip], developed an equation for describing the mass transfer to a gas bubble from molten metals at reduced pressures. Here it was assumed that the pressure inside the bubble was identical to the pressure inside the adjacent liquid. This is unlikely to be valid in the immediate vicinity of the free surface held at a low pressure. It was found that significant distortion of the bubble occurred on approaching the free surface; further more the observed expansion was much less than what one could expect from hydrostatic considerations. In their physical model, the authors assumed that bubble rises with a constant velocity and it maintains sphericity throughout the rise even after expansion.

Chao [69Cha] studied the transient heat and mass transfer to a translating fluid sphere at high Reynolds number. Major assumptions used in that analysis were irrotational flow field, constant properties, and thin boundary layers. From a similarity analysis, the average, outside Nusselt number at steady state was shown to be

$$Nu_{1, ss} = (2/\pi)^{1/2} Pe^{1/2} \quad (1.15)$$

while studying heat transfer between a vapor bubble in motion and the liquid, Ruckenstein also obtained identical results as Chao. Chao found that for sufficiently large Reynolds and Peclet numbers the transient response behavior of the thermal/species boundary layers of a circulating fluid sphere depends on a single parameter $U\epsilon/R$ and is independent of fluid properties. This is in contrast to that for the laminar boundary layers at the front stagnation of a solid sphere. He concludes that the growth of the boundary layer inside the fluid sphere is dominated by the diffusion process and is thus governed by the conduction transients. For mass transfer also an exactly similar approach was

used with heat flux substituted by mass flux and Nusselt number by Scherood number.

Levich [62Lev] examined the steady mass extraction rate from a spherical droplet of radius R falling at a constant velocity U in another liquid in the creeping flow regime. The velocity fields both inside and outside were those of Hardmard-Rybczynski [78Cli]. The Peclet numbers for mass transfer were assumed to be large and the transfer resistances on both sides of the droplet surface were comparable in magnitude. Levich had also analyzed the transient response behavior of the concentration boundary layers of the translating droplet and stated that the time required to attain steady state is $[1 + \mu^*] R/2 U$ where μ^* is the ratio of the inside and outside viscosities.

1. 5. SCOPE OF THE PRESENT STUDY:

In the present work, buoyancy-driven motion of a deformable bubble through a liquid metal bath during copper conversion has been studied. In addition to being an inherently interesting physical problem, the motion of deformable bubbles also represents a good example of the important class of free boundary problems in fluid mechanics, from which one may develop a better understanding of both the solution methods and the factors that control the boundary shape. The shape is dependent upon the viscous and pressure forces generated by the fluid motion. In this case, the shape of the boundary and the form of velocity and pressure fields in the fluid are intimately connected, and the boundary shape has been solved as a part of the overall solution of the problem. The flow field has been studied both inside and outside. The Finite element and finite difference methods have been used in combination for the analysis of flow and heat transfer in both phases.

While earlier studies used domain transformation for solving the shape, here simple finite difference technique has been used to solve for the bubble shape. The changes in the bubble volume and the translational velocities during the rise of the bubble are taken into account. The volume change is calculated from the prevailing hydrostatic pressure of the metallic bath at

any depth, assuming the entire bath to be isothermal. The change in the bubble velocity is determined by incorporating an instantaneous balance between the drag and buoyancy force acting on the bubble.

The finite element grid generation for this problem has been handled by the transfinite interpolation scheme. Though the study has been done for a single bubble it can be extended for multi-bubble system also. In addition to the analysis of shape and flow field, the mass transfer of reacting species both inside and outside has also been studied. Though the usual bubble shapes in metallic baths are of spherical cap geometry, it has not been practicable to simulate these conditions numerically when the shape distortion is severe. However, the simulation has been successfully carried out for considerably distorted ellipsoidal bubbles with an equivalent diameter less than or equal to 5 mm.

CHAPTER-II

MODEL FORMULATION

It has been experimentally proved that in different regimes of Reynolds number and Eötvös number, the bubble takes different shapes. But the basic question is why should the bubble have any resemblance to a spherical shape at all ? This is because of the dominant influence of surface tension forces, for small size bubbles. Surface tension always tend to reduce the surface area of free mass of fluid to the smallest value possible. The smallest possible surface area for a given volume is that of a sphere, and an isolated bubble or drop which is not distorted by external forces is pulled by uniform surface tension into a spherical shape. In terms of thermodynamics, the interface adjusts itself to the spherical shape in order to minimize its surface free energy.

This question also can be considered in terms of pressure, i. e. the pressure field prevailing in the surrounding fluid. The smaller the radius, the greater is the pressure difference between the two sides of the convex surface. For example, a cloud droplet of one micron radius has an internal pressure of more than two atmospheres. If the isolated bubble should momentarily assume some shape other than that of a sphere, its surface would have different radii of curvature at different points and the internal pressure just below the surface would momentarily be dissimilar at these various points. The consequent pressure gradients within the bubble would tend to force air from the regions of sharp surface curvature. This is equivalent to saying that surface tension, through its control of internal pressure, reshapes the bubble into a sphere whenever it happens to become slightly deformed. When the bubble is finally brought into the shape of a perfect sphere, the uniform surface curvature makes the pressure difference uniform at all points of its surface, and the internal pressure within the bubble is also uniform, provided the pressure field around the bubble remains so.

The disturbing effects on bubble shapes that appear, as one considers larger and larger bubbles, seem to be almost entirely due to dynamic and gravitational forces.

It is well known that when an object moves in a fluid the pressure just in front of the object becomes higher than average and the pressure in the rear region lower than the average. This means of course, that the internal pressure within a bubble or drop must change accordingly, the bubble develops an excess of pressure near its bottom and a deficiency of pressure all around its waist. And if one momentarily assumes that the fluid flow is that of a perfect fluid, there will be an excess of pressure near the top of the bubble as well as near the bottom.

The mechanism by which the shape of the bubble gets suitably adjusted is as follows. The gradients of internal pressure drive air from near the base and top out into the regions around the waist, thereby tending to flatten the bubble with an increase in the horizontal diameter. Even more intriguing is the fact that the resultant modification of the bubble surface curvature is just of the right kind required to help the bubble restore a uniform internal pressure and achieve an equilibrium. The sharpening of the curvature around the waist adjusts the surface tension effects to make up for the deficiency of external pressure there, while the flattening of curvature near the base and top tend to cancel the effects of the excessive internal pressure in those regions. Together, the joint action of surface tension and dynamic forces deforms the bubble continuously until it reaches a stable internal pressure distribution.

Now it may seem that a large bubble has truly brought itself into complete mechanical equilibrium when its internal pressure is uniform. But it must still meet an important demand, that of the hydrostatic head, that is the bubble must develop a vertical pressure gradient in such a way as to satisfy the familiar hydrostatic equation relating liquid density, liquid depth, and acceleration of gravity. This is quite prominent in a high density metallic bath as considered in the present study.

2.1 Assumptions of the model:-

The following simplifying assumptions are made in the development of the model.

(a) One isolated bubble surrounded by the matte is the system considered.

(b) The bubble motion is nearly steady. A coordinate frame (non-accelerating) attached to the bubble center is considered. In this coordinate frame the bubble is stationary and the fluid is flowing past the bubble in the direction opposite to bubble motion.

(c) The flow system possesses axial symmetry.

(d) The mass diffusivity, density, viscosity and surface tension of the gas and the matte are independent of temperature and concentration.

(e) The reaction at the interface is mass transfer controlled.

(f) At bubble surface, the surface shear stress is zero, because of the large difference in viscosities of the two fluids.

(g) The bath is isothermal, because of high the conductivity of the matte.

(h) The bubble surface is free from impurities.

(i) There exists a species boundary layer in the matte phase near the bubble interface, because of the large peclet number for the liquid.

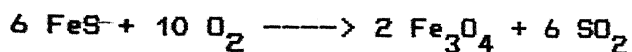
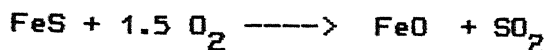
An isolated bubble has been considered here. But in a practical situation the system consists of many bubbles. Hence the flow field of one bubble may influence the other. Though the flow domain has been considered to be large, it may be compressed by suitable correction for the velocities at the

established boundary of the flow domain according to the celebrated cell model approach. (for details see appendix-3.)

In order to calculate the shape we must consider the bubble surface as a moving boundary. In this case the shape of the boundary and the velocity and pressure field distributions are intimately connected and one must solve the shape as a part of the solution. Since the bubble expands as it rises through a column of liquid, its motion and shape are not steady. To simplify the analysis we have assumed a quasi-steady rise of the bubble so that the buoyancy and the drag acting on the bubble nearly match each other. From this balance, the bubble velocity can be calculated as a function of instantaneous size. For the ease of computation, a coordinate frame which moves with the bubble is considered. Once the flow is established and shape is determined at a height then the distance traveled in that time step is predicted and the flow and other calculations are done in a quasi-static fashion till the O_2 in the bubble is exhausted completely.

The mass diffusivity, density, viscosity and surface tension change with temperature and the composition of the medium. Since much information is not available about the mass diffusivity, surface tension and the viscosity data of the system, some of the data have been considered in the near order of magnitude only. For the effect of change in temperature and composition see appendix-2.

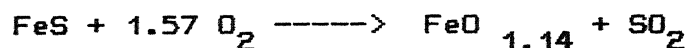
In the slag making stage, FeS is oxidized preferentially over Cu_2S according to the reactions:



The relative proportion of oxygen consumed and SO_2 produced within the air bubbles are determined by the stoichiometry of these reactions and the extent to which each occur

If the composition of the converter slag is known, an

overall reaction can be obtained from a combination of the above two reactions. For a slag containing 23% Fe_3O_4 and 30% FeO , simple mass balance gives the overall slag making reaction as:-



since the molar ratio of oxygen to iron is 1.14 in the slag. At high temperatures of conversion, the intrinsic rate of this reaction will be very fast and hence mass transport is likely to be the rate controlling step. Its equilibrium constant is extremely large. Therefore the reaction rate must be controlled by transport of one or more species, i. e. FeS in the liquid phase or O_2 in the gas phase. Same arguments hold good for the copper making stage also.

It is easily shown that the transport of FeS to the bubble matte interface will be rate controlling step if

$$C_{\text{FeS}}^b < 1/1.57 \left[\frac{K_{\text{O}_2}}{K_{\text{FeS}}} \right] C_{\text{O}_2}^b$$

Such a condition may be prevailing at the end of the slag making process. Similarly, for initial stages O_2 transfer within the bubble will govern the reaction kinetics if

$$C_{\text{FeS}}^b > 1/1.57 \left[\frac{K_{\text{O}_2}}{K_{\text{FeS}}} \right] C_{\text{O}_2}^b$$

where K = mass transfer co-efficient

C^b = bulk concentration

Both the transport step will be rate determining under the condition that

$$C_{\text{FeS}}^b = 1/1.57 \left[\frac{K_{\text{O}_2}}{K_{\text{FeS}}} \right] C_{\text{O}_2}^b \quad (\text{in between})$$

The stoichiometry of the blister making reaction indicates that certain volume of oxygen removed from the bubble due to reaction is replaced by the same volume of SO_2 . Hence the consumption of oxygen has no effect on bubble size during blister making.

The actual reaction nature has not been reported in

detail. Since the reaction constant is not available in literature the reaction at the interface is assumed to be mass transfer controlled. If a suitable reaction constant is made available the model will not change drastically and the only changes will be incorporation of a source or sink in the mass transport equation. For outside it is assumed that there exists a mass boundary layer since the mass peclet number is quite high (in order of 10^7). Beyond the boundary layer uniform concentration prevails in the matte.

Traces of surface active contaminants may have profound effects on the behavior of the bubble, even if the amount of impurity is so small that there is no measurable change in the bulk fluid properties. The contaminants cause drastic effects such as:

(i) Retardation of internal internal circulation there by rendering the interface rigid. Also the drag is significantly increased and the transport rates are decreased. (ii) Surfactants have greatest influence on terminal velocity near the point of transition from rectilinear to oscillating motion. This is presumably because internal circulation can drastically alter the wake structure of the fluid particle tending to delayed boundary layer separation, smaller wakes and delayed vortex shedding.

(iii) Surfactants play a particularly important role in high surface tension systems since surface tension reduction with contamination is largest for these systems.

2. 2. Governing Equations and Boundary Conditions:-

Consider the quasi-static rise of a bubble in a large bath of liquid. Axisymmetry about the direction of motion of the bubble has been assumed in this study and cylindrical coordinates are employed for convenience.

Since the pressure is a very important parameter for the deformation of the bubble the flow solution is obtained directly by u , p and v formulation of the Navier-Stokes equations and the continuity equation. The governing equations can now be written in vectorial form as:

$$\nabla \cdot V = 0 \quad \text{----- (2.1)}$$

$$\rho (\underline{V} \cdot \nabla V) = -\nabla p + \rho g + \mu (\nabla^2 V) \quad \text{----- (2.2)}$$

$$\text{where } \nabla = \frac{\partial}{\partial r} \hat{r} + \frac{1}{r} \frac{\partial}{\partial \theta} \hat{\theta} + \frac{\partial}{\partial z} \hat{k}$$

and V stands for u and v velocities in z & r directions respectively.

Though the flow achieves nearly a steady state very soon, the species transport is only unsteady in nature. The unsteady state mass transport equation in the absence of any source or sink term is given by

$$\frac{\partial X_A}{\partial t} + (V \cdot \nabla X_A) = D \nabla^2 X_A \quad \text{----- (2.3)}$$

where X_A stands for the mole fraction of any reacting species i. e. Cu_2S , FeS or O_2 & D stands for the diffusivity of the phase considered. For the liquid phase, the diffusivity is very small resulting in a large value of the mass Peclet number. Due to this the concentration varies in a thin layer adjacent to the bubble surface. In this region, the gradient of concentration normal to the bubble surface is much larger than the gradient parallel to the surface. The thin concentration boundary layer approximation consists of neglecting diffusion parallel to the surface in comparison to the diffusion normal to the surface. Defining $y = r - \bar{R}$, equation 2.3 can be simplified as:

$$\frac{\partial X_A}{\partial t} + (V \cdot \nabla X_A) = D \frac{\partial^2 X_A}{\partial y^2} \quad (2.4)$$

Formally, the above approximation requires $Pe \rightarrow \infty$, which for most practical situations means $Sc \rightarrow \infty$ for any finite Reynolds number. Surprisingly this approximation is often reasonable [78Cli] down to Sc of the order of unity. Use of the thin concentration boundary layer approximation is sometimes called the asymptotic solution for $Sc \rightarrow \infty$, since it is not

required that Re be large or that the momentum boundary layer approximation be made.

The representation of the boundary layer adjacent to the bubble and the appropriate coordinate system are sketched in figure 2.1. The x -coordinate is parallel to the surface, ($x=0$ at the front stagnation point), while the y -coordinate is normal to the surface. The distance from the axis of symmetry to the surface is R . It can easily be shown that even for a curved surface, the boundary layer equation takes the same form as that of a flat plate in terms of the curvilinear coordinates x and y . The final form of the mass transfer boundary layer equation is given by equation (2.4).

These equations are non-dimensionalized using the following parameters.

$$V^* = \frac{V}{U_{\infty}}, \quad \nabla^* = R \nabla, \quad p^* = \frac{p - p_{\infty}}{\rho U_{\infty}^2}, \quad \nu = \frac{\mu}{\rho}$$

$$Re = \frac{U_{\infty} R}{\nu}, \quad Fr^2 = \frac{U_{\infty}^2}{g R}, \quad X_A^* = \frac{X_A}{X_{A\infty}}$$

$$Pe = \frac{D}{R U_{\infty}}, \quad t^* = \frac{t}{t_c} = \frac{t D}{R^2}, \quad E\delta = \frac{\rho g R^2}{\sigma}$$

where

Re = Reynolds number

Pe = Mass pecllet number

Fr = Froud number

t_c = Characteristic time

R = radius of the bubble

ν = kinematic viscosity

U_{∞} = uniform velocity

$E\delta$ = Eötvös number

R = radius of equivalent spherical bubble

For the sake of comparison with experimental work, however the diameter of the equivalent spherical bubble (with the same volume) is selected for the reference length. The radius of equivalent bubble is defined as

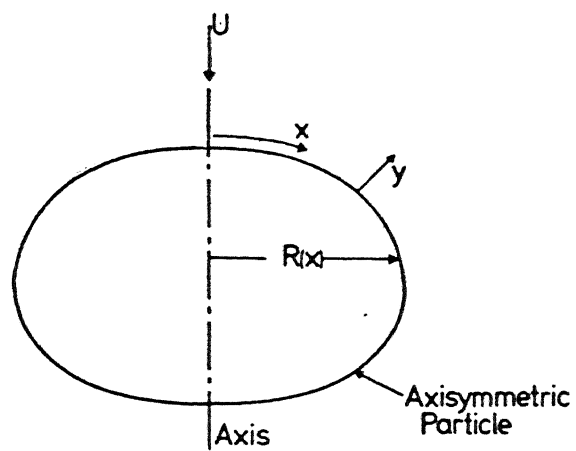


FIG. 2.1 Coordinates for the thin concentration boundary layer approximation

$$R = (3/4\pi V)^{1/3} \quad (2.5)$$

where V = volume of the bubble given by the expression

$$V = \frac{2\pi}{3} \int_0^\pi R^3(\theta) \sin \theta d\theta \quad (2.6)$$

The non dimensional form of the equations are as follows:

$$\nabla^* \cdot \mathbf{V}^* = 0 \quad (2.7)$$

$$(\mathbf{V}^* \cdot \nabla^* \mathbf{V}^*) = -\nabla^* p^* + \frac{1}{Re} (\nabla^{*2} \mathbf{V}^*) + \frac{1}{Fr^2} \quad (2.8)$$

$$\frac{\partial X_A^*}{\partial t^*} + Pe (\mathbf{V}^* \cdot \nabla^* X_A^*) = \nabla^{*2} X_A^* \quad (2.9)$$

$$u_x^* \left(\frac{\partial X_A^*}{\partial x^*} \right) + u_y^* \left(\frac{\partial X_A^*}{\partial y^*} \right) = \frac{1}{Pe} \frac{\partial^2 X_A^*}{\partial y^{*2}} \quad (2.10)$$

The following boundary conditions have been imposed to solve the governing equations (2.7 to 2.10) At infinity the liquid moves with a uniform velocity unity in the Z - direction. Numerical implementation of this condition requires that the region be cut at a certain $r = r_\infty$, this being of crucial importance for the efficiency of the calculation. This distance may be compressed by improving the condition in a manner that allows a good accuracy even if the solution domain is not very large (see appendix- 3). On the other hand the computational efficiency can be improved by generating the grid exponentially, through the transformation $r = e^z$.

In order to solve the Navier-Stokes equations in multi-phase problems, boundary conditions are required between the velocities on either side of the interface between the phases. The existence of an interface assures that the normal velocity in each phase is equal at the interface i. e.

$$V_n = (V_n)_p \quad (\text{everywhere on interface}) \quad (2.11)$$

where the subscript n refers to the direction normal to the interface. For bubbles of constant shape and size the normal velocity is zero with respect to the origin fixed to the bubble. The condition of tangential velocity continuity at the interface due to no slip condition takes the form

$$V_t = (V_t)_p \quad (\text{everywhere on interface}) \quad (2.12)$$

For fluid particles, two additional boundary conditions are provided by Newton's third law which requires that normal and shearing stress be balanced at the interface separating the two fluids.

The interface between two fluids is in reality a thin layer, typically a few molecular dimension thick. The thickness is not well defined since physical properties vary continuously from the values of one bulk phase to that of the other. In practice however, the interface is generally treated as if it were infinitesimally thin i. e. as if there were a sharp discontinuity between two bulk phases. Of special importance is the property of inter-facial tension σ , which is best viewed as the surface free energy per unit area at constant temperature.

A complete treatment of inter-facial boundary conditions in tensor notation is as follows. If surface viscosities are ignored the stress condition reduces to

$$p_p + (\tau_{nn})_p - p - \tau_{nn} = \sigma k \quad (2.13)$$

where k is curvature of the surface and τ_{nn} are the deviatoric normal stresses. Under static conditions the above equation reduces to Laplace equation. The tangential stress balance leads to

$$\tau_n + (\tau_{nt})_p = \nabla_s \sigma \quad (2.14)$$

where τ_{nt} and τ_n refer to the shearing stresses and ∇_s is the

surface gradient. The gas inside the bubble is in-viscid ($\mu_g \ll \mu_l$) and the surface exhibits no intrinsic shear or dialational viscosities. Also, usually there is no variation of surface tension on the bubble surface if the surface is not very much contaminated by surfactants. As a result, the tangential components of the stress vector have to be nearly equal to zero at the bubble surface.

$$\tau_{n+} = 0$$

On the same ground equation-2.13 reduces to

$$p_p - p + 2\mu \frac{\partial v_n}{\partial n} = \sigma k \quad (2.15)$$

As already said earlier the air from a high pressure region is driven to a region of low pressure in order to maintain an equilibrium or uniform thermodynamic pressure inside the bubble. Therefore, the internal pressure variation may be ignored and the resulting form of Laplace equation becomes

$$-p + 2\mu \frac{\partial v_n}{\partial n} = \sigma k \quad (2.16)$$

From differential geometry of surface revolutions, the curvature of an arbitrary surface can be defined in terms of radius and θ in spherical coordinate. (For detail see appendix-1)

$$k = \frac{R^2 + 2R'^2 - R R''}{(R^2 + R'^2)^{3/2}} + \frac{|R' \cos \theta - R \sin \theta|}{R \sin \theta (R + R')^{1/2}} \quad (2.17)$$

Now using this relation, the Laplace equation becomes

$$-p + 2\mu \frac{\partial v_n}{\partial n} = \sigma \left[\frac{R^2 + 2R'^2 - R R''}{(R^2 + R'^2)^{3/2}} + \frac{|R' \cos \theta - R \sin \theta|}{R \sin \theta (R + R')^{1/2}} \right] \quad (2.18)$$

Non dimensionalisation of this equation results in

$$-p^* + \frac{2}{Re} \frac{\partial v_n^*}{\partial n^*} = \frac{1}{E\delta} \left[\frac{R^{*2} + 2R^* \frac{\partial}{\partial n^*} R^*}{(R^{*2} + R^{*2})^{3/2}} + \frac{|R^* \cos \theta - R^* \sin \theta|}{R^* \sin \theta (R^{*2} + R^{*2})^{1/2}} \right] \quad (2.19)$$

This is the fundamental equation which determines the shape of the bubble the condition of tangential stress equal to zero condition gives the following relation. The tangential stress on any arbitrary surface can be defined as

$$\tau_s = \frac{(\sigma_{xx} - \sigma_{yy})}{2} \sin 2\alpha + \tau_{xy} \cos 2\alpha \quad (2.20)$$

(see figure 2.2)

where $\sigma_{xx} = -p + 2\mu \frac{\partial u}{\partial x}$ and $\sigma_{yy} = -p + 2\mu \frac{\partial v}{\partial y}$

$$\tau_{xy} = \mu \left(\frac{\partial u}{\partial y} + \frac{\partial v}{\partial x} \right)$$

$$\tau_s = - \left[\frac{2\mu (\frac{\partial u}{\partial x} - \frac{\partial v}{\partial y})}{2} \right] \sin 2\alpha + \mu \left(\frac{\partial u}{\partial y} + \frac{\partial v}{\partial x} \right) \cos 2\alpha$$

$$= 0$$

or

$$\left(\frac{\partial v}{\partial y} \sin 2\alpha + \frac{\partial v}{\partial x} \cos 2\alpha \right) + \left(\frac{\partial u}{\partial y} \cos 2\alpha - \frac{\partial u}{\partial x} \sin 2\alpha \right) = 0 \quad (2.21)$$

where α is the angle between the outward normals at any surface

The velocity with which the bubble rises up is also a function of the drag co-efficient and the buoyancy force on the bubble. The drag contribution comes from two sources, namely, the viscous drag and the form drag. As the geometry is changing, this force also changes causing a change in the velocity of rise. This can be expressed as

$$C_D = 8/3 (1 - \rho_g/\rho_l) gR/U^2 \quad (2.22)$$

The drag force exerted on the bubble surface is of the form

$$F_D = \left[\int_0^\pi \hat{i} (\sigma \cdot n) ds \right] \quad (2.23)$$

$$F_D = \left[\int_0^\pi (\sigma_{xx} \cos \alpha + \sigma_{xy} \cos \beta) ds \right] \quad (2.24)$$

$$\sigma_{xx} = -p + 2\mu \partial u / \partial x$$

$$\sigma_{xy} = \mu (\partial u / \partial y + \partial v / \partial x)$$

$$F_D = \left[\int_0^\pi (-p + 2\mu \partial u / \partial x) \cos \alpha + \mu (\partial u / \partial y + \partial v / \partial x) \cos \beta \right] ds \quad (2.25)$$

where $\cos \alpha$ and $\cos \beta$ are the direction cosines of the normal to the surface ds .

Non dimensionalised form of the expression is as follows

$$F_D / (1/2 \rho U^2) \pi \bar{R}^2 = C_D =$$

$$2 \left[\int_0^\pi (-p^* + 2/Re \partial u^* / \partial x^*) \cos l x + 1/Re (\partial u^* / \partial y^* + \partial v^* / \partial x^*) \cos l y \right] y^* dl \quad (2.26)$$

$$\text{where } p^* = p / \rho U^2$$

Computing C_D the change in the velocity of bubble rise can be predicted. Both U_∞ and \bar{R} of the bubble will change during the upward rise, and so also the Reynolds number.

The fact that mass transport is the rate controlling step gives rise to the condition that,

$$X_A = 0$$

at the interface for all time steps. In addition, the mass transfer boundary conditions are:

$$X_A^* = 1.0 \quad \text{at all other points inside the bubble at } t = 0 \quad \text{i.e.} \quad X_A^* = 0 \quad \text{at } Y = 0 \quad \text{and } X_A^* = 1 \quad \text{as } y \rightarrow \infty$$

The governing equations and boundary conditions above have been solved in a coupled manner using the Finite element method. The details of the solution procedure are described in the next chapter.

CHAPTER III

SOLUTION PROCEDURE

Analytical solution of the governing equations presented in chapter-II is not possible. Hence certain numerical schemes have been used. Before solving a physical problem on a digital computer, one has to decide which scheme is to be used for computation. Variety of numerical techniques are available such as Finite difference, Finite element and Finite volume method for solving these equations. In the present problem the geometry of the physical domain is not regular. In addition to that the parameter of importance for shape calculation is pressure and velocity. Therefore Finite element method is considered to be the most suitable technique for obtaining velocity profile and pressure directly for this irregular moving boundary problem. While the flow calculation is done using finite element method, finite difference method is used for the shape calculation from Laplace equation and for the solution of the concentration boundary layer in the liquid phase. Therefore the solution procedure involves both FEM and FDM in combination.

3. 1. FEM Analysis:

In FEM, the governing differential equations are converted into equivalent set of integral equations which are minimized over the whole solution domain. The solution domain is divided into several small elements of known shape and solution variable is approximated within each of these elements by suitable approximation of functions. The integral equations are then evaluated within each element using the approximating functions and all such elemental integrals are assembled to obtain the final matrix equations to be solved. Two procedures are available for converting the governing partial differential equations for equivalent integral equations. These are

- (a) Variational Procedure
- (b) Galerkin's Procedure

In the present work, Galerkin's approach is used. The Galerkin's technique is one among the class of techniques collectively known as the method of Weighted residuals [77Zie]. This procedure is used on the fact that, for the differential equation of the form

$$L(\phi) = 0 \quad (3.1)$$

where ϕ is the exact solution to the differential equation, an approximation ϕ^* will leave behind a residue. That is

$$L(\phi^*) = R \quad (3.2)$$

where R is the residue, which may be a function of spatial coordinate and time. In Galerkin's procedure, the residue weighted appropriately by suitable weighting functions is minimized over the whole solution domain D . In mathematical form, this becomes

$$\int_D W_i R \, dv = \int_D W_i L(\phi^*) \, dv = 0 \quad (3.3)$$

for each i , where W_i are weighting functions. The approximation function ϕ^* may be written as a piece continuous profile for each element as

$$\phi^*(e) = \sum_{i=1}^m N_i(e) \phi_i^{(e)} \quad (3.4)$$

In the above equation, m is the number of nodes per element and $N_i^{(e)}$ are the interpolating functions or shape functions of the elements. The nodal values of ϕ^* for the element are denoted by $\phi_i^{(e)}$. In Galerkin's procedure, the weighting function W_i are taken to be the same as the shape functions $N_i^{(e)}$ within each element.

3. 2. Types of formulations:

There are four types of formulations which are in use for obtaining finite element solutions of any flow problem. Those are:

- (1) Stream function formulation.
- (2) Stream function and Vorticity formulation.
- (3) Penalty formulation.
- (4) Velocity Pressure formulation.

The stream function approach for solving the flow

problem was first proposed by Oslon[750sl]. By introducing the stream function ψ , the continuity equation can be satisfied exactly and the momentum equation can be combined into a single function in terms of ψ . The main disadvantage of this formulation is that the governing equations and the interpolating functions of higher order are required. Also in order to get velocity and pressure, further processing is required.

In stream function-vorticity formulation, in stead of dealing with a single governing equation of fourth order, the stream function(ψ) and vorticity(ω) are chosen as the unknowns and two governing equations of second order in ψ and ω result [73Tay]. In this formulation, the boundary conditions may consist of specified values of ψ and ω or specified values of their first derivatives. The principal difficulty in using the stream function-vorticity formulation is that, in general, vorticity is unknown a priori along the boundaries.

In penalty function [78Hen] approach, pressure variable is eliminated and only the velocity components are solved. This approach is sometimes useful because retaining pressure as a variable often leads to numerical difficulties. The penalty formulation involves treating continuity equation as a constraint among the velocity components and the continuity constraint is introduced into the momentum equation in a Lagrange multiplier λ . It is possible to choose λ to be very large and eliminate the pressure in terms of λ . The boundary conditions to be specified for this formulation are either specified values of velocity components or specified values of their first derivatives.

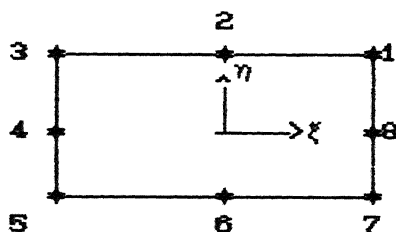
In velocity pressure formulation, the pressure and velocity components are considered as the nodal variables. The advantages of this formulation are :

- (1) The formulation is readily extended to three dimension.
- (2) Only C^0 (linear element) continuity is required for element interpolation functions.
- (3) Pressure, velocity, velocity gradient and shear boundary conditions can be directly incorporated into the matrix equations.
- (4) Free surface problems are tractable.
- (5) The formulation takes less computational time than the stream function vorticity formulation.[73Tay]

In the present study, this approach is used because the primitive variables are obtained directly.

3.3 DERIVATION OF FINITE ELEMENT EQUATION :

The discretized domain is shown in fig-3.1a & 3.1b. The elements used through out the work is the isoparametric quadrilaterals containing eight nodes, one at each corner and one at the midpoint of each side (see fig-3.2). In general terms parabolic element is one which can accommodate a parabolic variation in the variables along any side of and across the element. The term isoparametric implies that both elemental geometry and variation in the variables across the elements are described using the same type of polynomial or shape function. Since the element sides can follow parabolic shapes then quite complicated physical geometries can be mapped with few such elements.



(Fig - 3.2) Eight noded isoparametric element.

Under most circumstances the utilization of normalized coordinates standardizes the integration process. For example consider a general form of equation in terms of global coordinates

$$\int \int_{\Omega} F'(x,y) dx dy \quad (3.5)$$

or introducing the limits of integration

$$\int_{x_a}^{x_b} \int_{y_a}^{y_b} F'(x,y) dx dy \quad (3.6)$$

for one element it can be written in terms of normalized

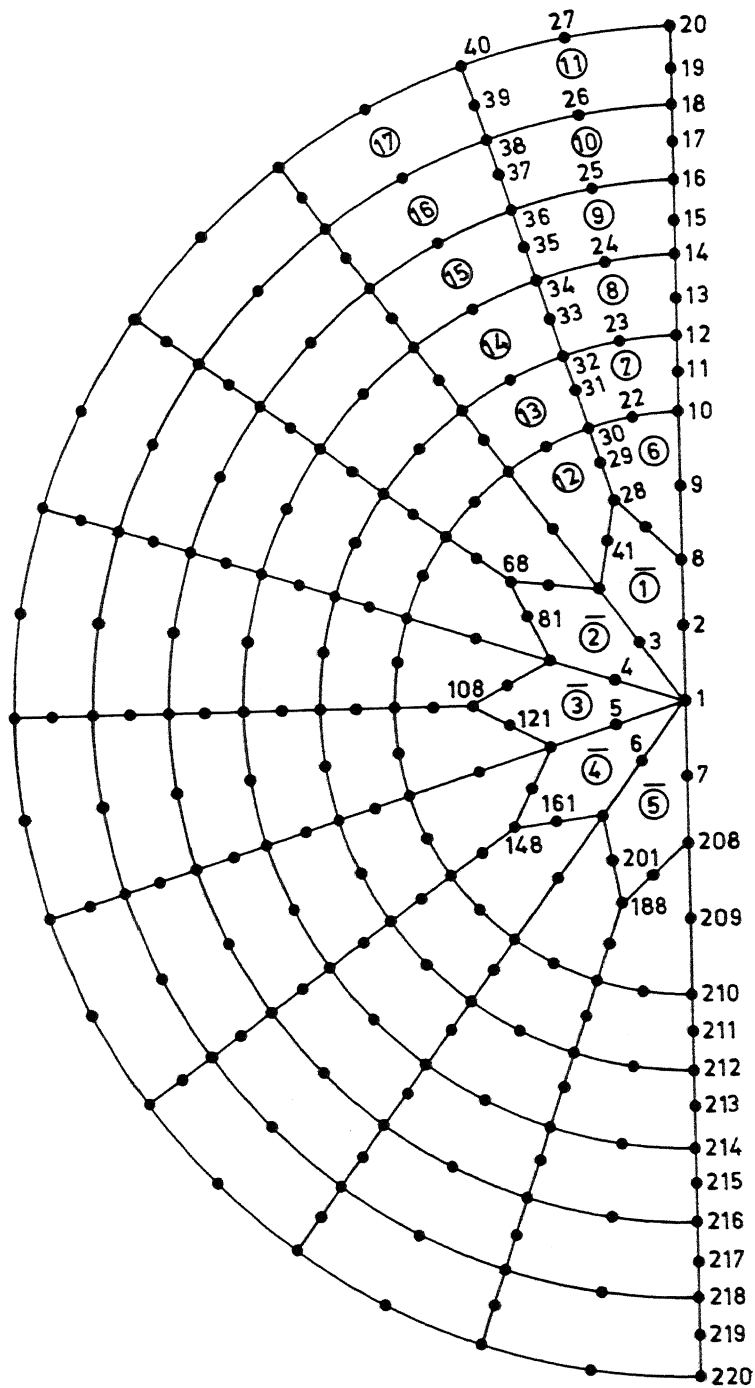


FIG. 3.1b. INSIDE GRID STRUCTURE

N NODE NUMBER
 ⓪ AUTOMATICALLY GENERATED ELEMENT NUMBER
 ⓪ FIXED SET OF ELEMENT NUMBER

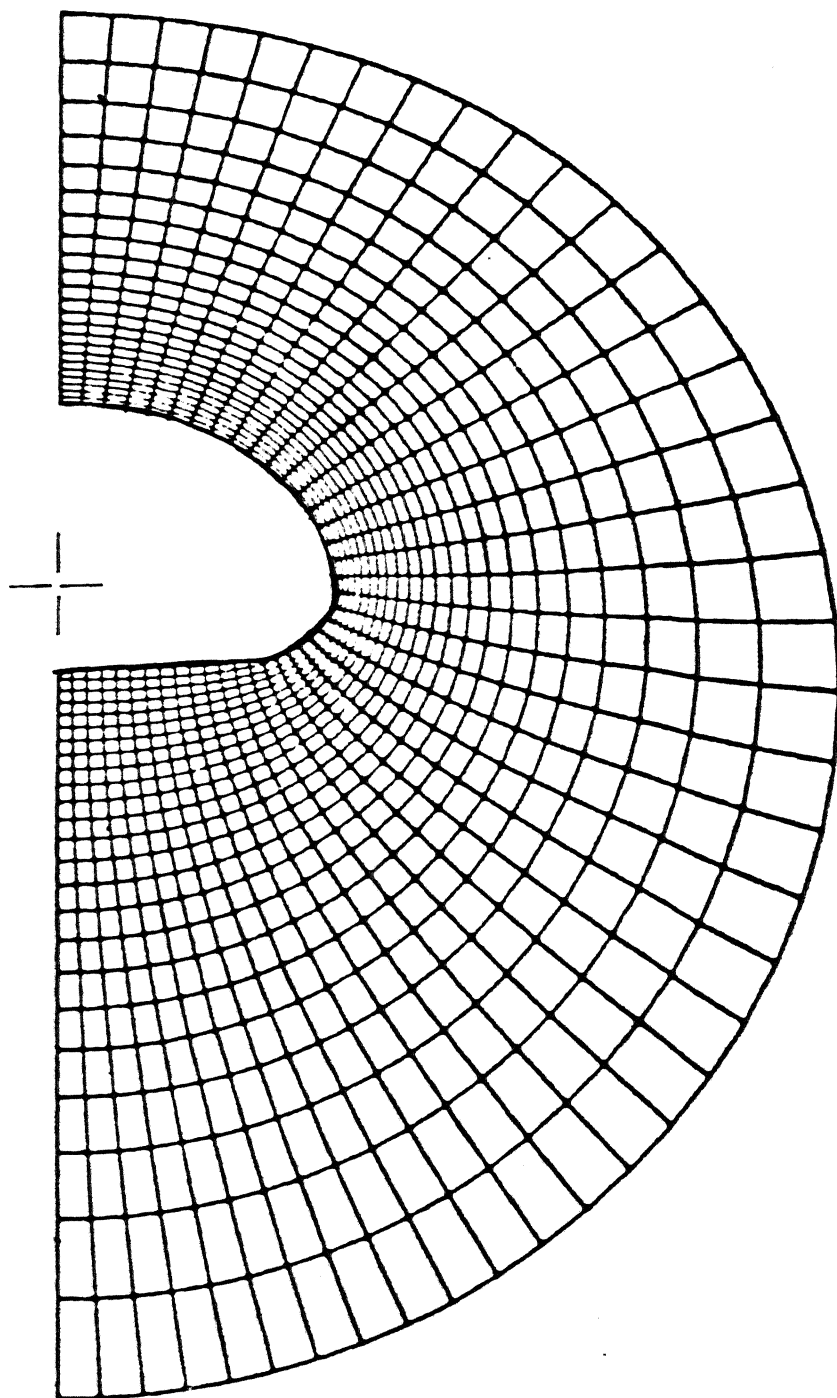


FIG. 3.1a. EXPONENTIALLY DISCRETIZED GRID FOR OUTSIDE.

curvilinear coordinates

$$\int_{-1}^{+1} \int_{-1}^{+1} F(\xi, \eta) d\xi d\eta \quad (3.7)$$

which can be integrated quite readily using simple integration techniques. A numerical integration procedure is adopted where the sampling points are termed as gauss points. In particular the Gauss-Legendre quadrature is used leading to a high accuracy. For example

$$I = \int_{-1}^{+1} \int_{-1}^{+1} F(\xi, \eta) d\xi d\eta \quad (3.8)$$

after implementing Gaussian integration

$$I = \sum_{i=1}^{n_{\text{gauss}}} \sum_{j=1}^{n_{\text{gauss}}} a_j a_i F(\xi_i, \eta_j) \quad (3.9)$$

n_{gauss} = number of gauss points

a_i & a_j are weighting factors

ξ_i and η_j are coordinates of the i^{th} and j^{th} integration points.

The shape functions

Corner nodes: $N_i = \frac{1}{4} (1 + \xi_i \xi) (1 + \eta_i \eta) (\xi_i \xi + \eta_i \eta - 1)$

Mid side nodes: $N_i = \frac{1}{2} (1 - \xi^2) (1 + \eta_i \eta) \quad , \xi = 0$

$$N_i = \frac{1}{2} (1 + \xi_i \xi) (1 - \eta^2) \quad , \eta = 0$$

Clearly if a local coordinate system is to be used then the first order variation with respect to the global coordinates must also be expressed in terms of local coordinates as:

$$\frac{\partial N_i}{\partial \xi} = \frac{\partial N_i}{\partial x} \frac{\partial x}{\partial \xi} + \frac{\partial N_i}{\partial y} \frac{\partial y}{\partial \xi} \quad (3.10)$$

$$\frac{\partial N_i}{\partial \eta} = \frac{\partial N_i}{\partial x} \frac{\partial x}{\partial \eta} + \frac{\partial N_i}{\partial y} \frac{\partial y}{\partial \eta} \quad (3.11)$$

$$\text{or, } \begin{bmatrix} \frac{\partial N_i}{\partial \xi} \\ \frac{\partial N_i}{\partial \eta} \end{bmatrix} = \begin{bmatrix} \frac{\partial x}{\partial \xi} & \frac{\partial y}{\partial \xi} \\ \frac{\partial x}{\partial \eta} & \frac{\partial y}{\partial \eta} \end{bmatrix} \begin{bmatrix} \frac{\partial N_i}{\partial x} \\ \frac{\partial N_i}{\partial y} \end{bmatrix} = J \begin{bmatrix} \frac{\partial N_i}{\partial x} \\ \frac{\partial N_i}{\partial y} \end{bmatrix} \quad (3.12)$$

$$\text{or, } \begin{bmatrix} \frac{\partial N_i}{\partial x} \\ \frac{\partial N_i}{\partial y} \end{bmatrix} = J^{-1} \begin{bmatrix} \frac{\partial N_i}{\partial \xi} \\ \frac{\partial N_i}{\partial \eta} \end{bmatrix} \quad (3.13)$$

J=Jacobian evaluated explicitly since the local variation in x and y can be defined.

$$J = \begin{bmatrix} \sum_{i=1}^8 \frac{\partial N_i}{\partial \xi} x_i & \sum_{i=1}^8 \frac{\partial N_i}{\partial \xi} y_i \\ \sum_{i=1}^8 \frac{\partial N_i}{\partial \eta} x_i & \sum_{i=1}^8 \frac{\partial N_i}{\partial \eta} y_i \end{bmatrix} \quad (3.14)$$

$$dx \, dy = \det J \, d\xi \, d\eta$$

In the present work, the primitive variables u, p and v are evaluated from the solution of coupled Navier-Stokes and continuity equation iteratively. The procedure is then to assume a starting value or initial guess for u, v and p then solve for these variables till the solution is converged.

Following the accepted practice of depicting the variation of pressure by shape functions of one order lower than those for defining the velocity distribution [81Tay]

$$u = \sum_{i=1}^n N_i u_i$$

$$v = \sum_{i=1}^n N_i v_i$$

$$p = \sum_{i=1}^m N_i p_i$$

where $n = 8$ and $m = 4$

This requirement is effected by utilizing the same element geometry where all eight nodes are associated with velocities and only corner nodes with pressure. Spatial coordinates within the element are defined in terms of all eight nodes. This element is called superparametric when fewer nodes are used to define a variable other than the spatial coordinates.

Employing the Galerkin's weighted residual approach, eq.2.1 and 2.2 result in

$$\sum_1^{n_e} \int_{\Omega} \left[N_i \nabla \cdot v \right] dV = 0 \quad (3.15)$$

$$\sum_1^{n_e} \int_{\Omega} \left[(v \cdot \nabla v) + \nabla p - \frac{1}{Re} (\nabla^2 v) \right] dV = 0$$

$$\text{or } \sum_1^{n_e} \left[\int_{\Omega} N_i (v \cdot \nabla v) dV + \int_{\Omega} N_i \nabla p dV - \int_{\Omega} \frac{N_i}{Re} [\nabla^2 v] dV \right] = 0 \quad (3.16)$$

The higher order derivatives require higher order shape functions or polynomials. They can easily be reduced into lower order by weak formulation.

$$\begin{aligned} \int_{\Omega} N_i (\nabla^2 v) dV &= \int_{\Omega} \nabla \cdot N_i (\nabla v) dV - \int_{\Omega} \nabla N_i \cdot \nabla v dV \\ &= - \int_{\Omega} \nabla N_i \cdot (\nabla v) dV + \int_{\Gamma} N_i (\nabla v) \cdot n d\Gamma \quad [\text{Green's Theorem}] \end{aligned}$$

The resulting equation becomes

$$+ \frac{1}{\text{Re}} \int_{\Omega} \left(\frac{\partial N_j}{\partial x} \sum_1^8 \frac{\partial N_j}{\partial x} \right) u_j dV + \frac{1}{\text{Re}} \int_{\Omega} \left(\frac{\partial N_i}{\partial y} \sum_1^8 \frac{\partial N_j}{\partial y} \right) u_j dV \quad (3.22)$$

On the boundary

$$\sum_1^8 \left(\frac{\partial N_j}{\partial y} \sin 2\alpha + \frac{\partial N_j}{\partial x} \cos 2\alpha \right) v_j d\alpha + \sum_1^8 \left(\frac{\partial N_j}{\partial y} \cos 2\alpha - \frac{\partial N_j}{\partial x} \sin 2\alpha \right) d\alpha = 0 \quad (3.23)$$

$$\sum_1^8 N_j \cos \alpha u_j d\alpha + \sum_1^8 N_j \sin \alpha v_j d\alpha = 0 \quad (3.24)$$

If $\cos \alpha > \sin \alpha$, then (3.24) is u-equation and (3.23) is v-equation and vice versa. Implementation of this condition gives diagonal dominance to the respective equation.

The shape deviates from sphericity. Hence the direction cosines are now functions of the surface revolution. They are to be evaluated on the surface itself. These outward normals are calculated in turn and different values are associated with different sides as follows.

y-component of outward normals

SIDE	$\cos lx$
1	$-\partial x / \partial \eta$
2	$-\partial x / \partial \xi$
3	$\partial x / \partial \eta$
4	$\partial x / \partial \xi$

x-component of outward normals

SIDE	$\cos ly$
1	$\partial y / \partial \eta$
2	$\partial y / \partial \xi$
3	$-\partial y / \partial \eta$
4	$-\partial y / \partial \xi$

The elemental side length are different for different locations. These are calculated as

the element side making up the boundary of the domain.

In the present study, the boundary condition have been applied directly using eq 2.11 and 2.21.

$$\left(\frac{\partial V}{\partial y} \sin 2\alpha + \frac{\partial V}{\partial x} \cos 2\alpha\right) + \left(\frac{\partial u}{\partial y} \cos 2\alpha - \frac{\partial u}{\partial x} \sin 2\alpha\right) = 0 \quad (3.18)$$

$$V_n = u \cos \alpha + v \sin \alpha = 0 \quad (3.19)$$

the expanded form of eq.3.15 to 3.18 are as follows:

$$\sum_1^{n_e} \left[\int_{\Omega} N_i \left(\sum_1^8 \frac{\partial N_j}{\partial y} + \sum_1^8 N_j \sum_1^8 N_k y_k \right) v_j dV + \int_{\Omega} N_i \sum_1^8 \frac{\partial N_j}{\partial x} v_j dV \right] = 0 \quad (3.20)$$

The y-component of the momentum equation is

$$\begin{aligned} \sum_1^{n_e} \left[\int_{\Omega} N_i \left(\sum_1^8 N_k v_k \sum_1^8 \frac{\partial N_j}{\partial y} + \sum_1^8 N_k u_k \sum_1^8 \frac{\partial N_j}{\partial x} \right) v_j dV \right. \\ \left. + \int_{\Omega} N_i \sum_1^4 \frac{\partial N_j}{\partial y} p_j dV - \int_{\Omega} N_i \frac{1}{Fr^2} dV \right. \\ \left. + \frac{1}{Re} \left[\int_{\Omega} \left(\frac{\partial N_i}{\partial y} \sum_1^8 \frac{\partial N_j}{\partial y} \right) v_j dV + \int_{\Omega} \left(\frac{\partial N_i}{\partial x} \sum_1^8 \frac{\partial N_j}{\partial x} \right) v_j dV \right] \right] = 0 \quad (3.21) \\ + \frac{1}{Re} \left[\frac{N_i \cdot N_j}{\gamma^2} \right] dV \end{aligned}$$

Similarly the x-momentum equation

$$\begin{aligned} \sum_1^{n_e} \left[\int_{\Omega} N_i \left(\sum_1^8 N_k v_k \sum_1^8 \frac{\partial N_j}{\partial y} + \sum_1^8 N_k u_k \sum_1^8 \frac{\partial N_j}{\partial x} \right) u_j dV \right. \\ \left. + \int_{\Omega} N_i \sum_1^4 \frac{\partial N_j}{\partial x} p_j dV - \int_{\Omega} N_i \frac{1}{Fr^2} dV \right] \end{aligned}$$

$$+ \frac{1}{Re} \int_{\Omega} \left(\frac{\partial N_j}{\partial x} \sum_1^8 \frac{\partial N_j}{\partial x} \right) u_j dV + \frac{1}{Re} \int_{\Omega} \left(\frac{\partial N_i}{\partial y} \sum_1^8 \frac{\partial N_j}{\partial y} \right) u_j dV \quad (3.22)$$

On the boundary

$$\sum_1^8 \left(\frac{\partial N_j}{\partial y} \sin 2\alpha + \frac{\partial N_j}{\partial x} \cos 2\alpha \right) v_j d\alpha + \sum_1^8 \left(\frac{\partial N_j}{\partial y} \cos 2\alpha - \frac{\partial N_j}{\partial x} \sin 2\alpha \right) d\alpha = 0 \quad (3.23)$$

$$\sum_1^8 N_j \cos \alpha u_j d\alpha + \sum_1^8 N_j \sin \alpha v_j d\alpha = 0 \quad (3.24)$$

If $\cos \alpha > \sin \alpha$, then (3.24) is u-equation and (3.23) is v-equation and vice versa. Implementation of this condition gives diagonal dominance to the respective equation.

The shape deviates from sphericity. Hence the direction cosines are now functions of the surface revolution. They are to be evaluated on the surface itself. These outward normals are calculated in turn and different values are associated with different sides as follows.

y-component of outward normals

SIDE	$\cos 1x$
1	$-\partial x / \partial \eta$
2	$-\partial x / \partial \xi$
3	$\partial x / \partial \eta$
4	$\partial x / \partial \xi$

x-component of outward normals

SIDE	$\cos 1y$
1	$\partial y / \partial \eta$
2	$\partial y / \partial \xi$
3	$-\partial y / \partial \eta$
4	$-\partial y / \partial \xi$

The elemental side length are different for different locations. These are calculated as

SIDE

1,3

2,4

LENGTH

$$\left[\left(\frac{\partial x}{\partial \eta} \right)^2 + \left(\frac{\partial y}{\partial \eta} \right)^2 \right]^{1/2}$$

$$\left[\left(\frac{\partial x}{\partial \xi} \right)^2 + \left(\frac{\partial y}{\partial \xi} \right)^2 \right]^{1/2}$$

The final assembled form of the equation is

$$[A] \{X\} = \{B\} \quad (3.25)$$

where $[X] = \begin{bmatrix} u_i \\ p_i \\ v_i \end{bmatrix}$

Each coefficient in the matrix $[A]$ has the form

$$a_{ij} = \sum_1^n \int_{A^e} \begin{bmatrix} c_{11} & c_{12} & c_{13} \\ c_{21} & c_{22} & c_{23} \\ c_{31} & c_{32} & c_{33} \end{bmatrix} dA$$

$$b_i = \sum_1^n \int_{A^e} \begin{bmatrix} b_1 \\ b_2 \\ b_3 \end{bmatrix} dA$$

where $c_{11} = N_i N_k u_k \frac{\partial N_j}{\partial x} + N_i N_k v_k \frac{\partial N_j}{\partial y} + \frac{1}{Re} \frac{\partial N_i}{\partial x} \frac{\partial N_j}{\partial x} + \frac{1}{Re} \frac{\partial N_i}{\partial y} \frac{\partial N_j}{\partial y}$

$$c_{12} = N_i \frac{\partial N_i}{\partial x}$$

$$c_{13} = 0$$

$$c_{21} = N_i \frac{\partial N_j}{\partial x}$$

$$c_{22} = 0$$

$$c_{23} = N_i \frac{\partial N_j}{\partial y} + \frac{N_j}{N_k y_k} N_i$$

$$c_{31} = 0$$

$$c_{32} = N_i \frac{\partial N_j}{\partial y}$$

$$c_{33} = c_{11} + \frac{1}{Re} \left[N_i N_i / y^2 \right]$$

$$b_1 = N_i \frac{1}{Fr^2}$$

$$b_2 = 0$$

$$b_3 = N_i \frac{l_{x2}}{Fr^2}$$

where l_{x1} and l_{x2} are direction cosines of the x and y global axes to the direction of the gravitational field.

On boundary, the coefficient matrix changes depending upon the equation which is being considered as u and v equations. The matrix equation is solved iteratively by Frontal method. (For detail see appendix-4).

Once the primitive variables are obtained, the shape of the bubble is predicted from the Laplace's equation. This equation is highly nonlinear due to the presence of first and second order derivatives of function $R(\theta)$. Hence it has to be solved iteratively. The construction of the difference approximation was really challenging, because of the instable nature of the equation. The aim was to obtain as implicit as possible a scheme in order to decrease the jump of the solution vector. The following quasi linear form was successful to get a converged solution of the function $r = R(\theta)$. One fictitious time step was introduced. The simplified form of the equation is as follows.

$$-p_0 + 2\mu \frac{\partial v_n}{\partial n} = \frac{1}{E\delta} \left[\frac{1}{(R^2 + R'^2)^{1/2}} + \frac{R'^2 - R R''}{(R^2 + R'^2)^{3/2}} + \frac{|R' \cot \theta - R|}{R (R^2 + R'^2)^{1/2}} \right] \quad (3.26)$$

$$\text{or, } R'' = \left[\frac{1}{(R^2 + R'^2)^{1/2}} + \frac{R'^2}{(R^2 + R'^2)^{3/2}} + \frac{|R' \cot \theta - R|}{(R^2 + R'^2)^{1/2} R} - \Delta p E\delta \right] \frac{(R^2 + R'^2)^{3/2}}{R}$$

$$\text{or, } R'' - R = \left[\frac{2 R'^2}{R} + \frac{R^2 + R'^2}{R} |R' \cot \theta - R| - \frac{\Delta p E\delta (R^2 + R'^2)^{3/2}}{R} \right]$$

Now implementing the above said implicit scheme the resulting

form of the Laplace equation becomes

$$R^{k+1} - R^k = \left[\frac{2R^k + (R^k + R^k)}{R} + \frac{(R^k \cot \theta - R^k)}{\Delta p E_0 (R^k + R^k)^{3/2}} \right]^k$$

Introducing the difference equation, the resulting equation takes the form

$$R_{i+1} + R_{i-1} - 2R_i - R_i \Delta \theta^2)^{k+1} = \left[\frac{(R_{i+1} - R_{i-1})^2}{2R_i} + \Delta \theta^2 + (R_{i+1} - R_{i-1})^2 \left| \frac{R_{i+1} - R_{i-1}}{2\Delta \theta} \cot \theta_i - R_i \right| - \frac{\Delta p E_0}{R_i} \right]^k \quad (3.27)$$

As the function $R(\theta)$ is to be smooth at the axis of symmetry of the spherical coordinates, the boundary conditions for $R(\theta)$ are

$$\frac{dR}{d\theta} = 0 \text{ at } \theta = 0 \text{ and } \pi \quad (3.28)$$

which is approximated as

$$-3R_1 - 4R_2 - R_3 = 0 \quad -3R_N - 4R_{N-1} - R_{N-2} = 0$$

so that the equation comprise a tridiagonal system which is solved by using the Tridiagonal algorithm. Even this solution resulted in a monotonic increment of the solution vector for which an additional constraint was imposed on the solution for $R(\theta)$. This is the preservation of the dimensionless bubble volume namely

$$V = \frac{2\pi}{3} \int_0^\pi R^3(\theta) \sin \theta d\theta \quad (3.29)$$

from which the characteristic length scale of the problems, the equivalent bubble radius is determined as

$$a = \left(\frac{3V}{4\pi} \right)^{1/3} \quad (3.30)$$

The monotonic increment of the solution to $R(\theta)$ was arrested by dividing the function $R(\theta)$ by this equivalent radius "a" which is determined at each fictitious time step. Simpson's rule was used for determination of equivalent volume. Imposition of this

restriction on the solution of $R(\theta)$ is required because of the boundary condition.

Here we have $\frac{\partial R}{\partial \theta} = 0$ at $\theta = 0$ and π .

This is an over deterministic situation. In such a case the solution will involve an arbitrary constant which can not be uniquely determined. For example, let us consider an equation of the following form

$$R'' = \text{constant}$$

$$\text{Now, } R' = \text{constant } \theta + C$$

$$\text{But } R' = 0 \text{ at } \theta = 0 \text{ and}$$

$$R' = 0 \text{ at } \theta = \pi$$

Implementation of the boundary condition gives the following relation

$$0 = \text{constant } 0 + C$$

$$0 = \text{constant } \pi + C$$

Hence C can not be uniquely determined.

Once the shape and flow field both inside and outside are established the mass transport equation becomes linear.

Applying Galerkin's approach to eqn 2.9 the resulting equation is as

$$\sum_1^n \left[\frac{1}{Pe} \int_{\Omega} N_i \frac{\partial x_A}{\partial t} dV + \int_{\Omega} N_i (v \cdot \nabla x_A) dV - \frac{1}{Pe} \int_{\Omega} N_i \nabla^2 x_A dV \right] = 0 \quad (3.31)$$

Using weak formulation and Green's integration techniques

$$- \frac{1}{Pe} \int_{\Omega} N_i \nabla^2 x_A dV = \frac{1}{Pe} \left[\int_{\Omega} \nabla N_i \cdot \nabla x_A dV - \int_{\Gamma} N_i \nabla x_A \cdot n d\Gamma \right]$$

Since there is no gradient boundary conditions, the line integral term vanishes.

$$\sum_1^n \left[\int_{\Omega} \frac{1}{Pe} N_i \frac{\partial x_A}{\partial t} dV + \int_{\Omega} N_i v \cdot \nabla x_A dV + \frac{1}{Pe} \int_{\Omega} \nabla N_i \cdot \nabla x_A dV \right] = 0 \quad (3.32)$$

The transient mass transport equation for inside (Gas phase) is solved by Implicit Finite element method. The resulting equation is

$$\sum_1^{n_e} \left[\int_{\Omega} Pe N_i N_j \frac{\partial x_A}{\partial t} dV + \int_{\Omega} N_i \left(\sum_1 N_k u_k \sum_1 \frac{\partial N_j}{\partial x} + \sum_1 N_k v_k \sum_1 \frac{\partial N_j}{\partial y} \right) x_{A_j}^{k+1} dV + \frac{1}{Pe} \int_{\Omega} \left(\frac{\partial N_j}{\partial x} \sum_1 \frac{\partial N_j}{\partial x} + \frac{\partial N_i}{\partial y} \sum_1 \frac{\partial N_j}{\partial y} \right) x_{A_j}^{k+1} dV \right] = 0$$

$$\text{or, } \sum_1^{n_e} \left[\int_{\Omega} N_i \left(\sum_1 N_k u_k \frac{\partial N_j}{\partial x} + \sum_1 N_k v_k \frac{\partial N_j}{\partial y} \right) dV + \frac{1}{Pe} \int_{\Omega} \left(\frac{\partial N_j}{\partial x} \frac{\partial N_i}{\partial x} + \frac{\partial N_i}{\partial y} \frac{\partial N_j}{\partial y} \right) dV \right] \left[x_j^{k+1} \right] + \frac{1}{Pe} \int_{\Omega} N_i N_j dV \left[x_j \right] = \frac{1}{\Delta t} \left[x_j^{k+1} - x_j^k \right]$$

$$\text{or, } \sum_1^{n_e} \left[Pe \Delta t \left\{ \int_{\Omega} N_i \left(\sum_1 N_k u_k \frac{\partial N_j}{\partial x} + \sum_1 N_k v_k \frac{\partial N_j}{\partial y} \right) dV \right\} + \Delta t \left\{ \int_{\Omega} \frac{\partial N_i}{\partial x} \frac{\partial N_j}{\partial x} + \frac{\partial N_i}{\partial y} \frac{\partial N_j}{\partial y} \right\} dV \right] \left[x_j^{k+1} \right] + \left[\int_{\Omega} N_i N_j dV \right] \left[x_j^{k+1} \right] = \left[x_j^k \right] \left[\int_{\Omega} N_i N_j dV \right] \quad (3.33)$$

Similarly equation for mass boundary layer is solved where the $\partial x_A / \partial x$ term is considered as if the transient term and it is marched in x . Here x , is a fictitious time coordinate.

$$\frac{\partial x_A}{\partial x} = \frac{\pi}{Pe u_x} \frac{\partial^2 x_A}{\partial y^2} - \frac{\pi u_j}{u_x} \frac{\partial x_A}{\partial y}$$

$$\frac{\partial x_A}{\partial x} = C_1 x_{i+1} - C_2 x_i + C_3 x_{i-1} \quad (3.34)$$

$$\text{where } C_1 = \pi / (Pe u_x \Delta y^2)$$

$$C_2 = [\pi (Pe u_y \Delta y + 2)] / (\Delta y^2 Pe u_x)$$

$$C_3 = \pi (Pe u_y \Delta y + 1) / (Pe u_x \Delta y^2)$$

Drag coefficient is calculated by using the Gaussian quadrature formula. Similarly the consumption of oxygen is

estimated by integrating the mass flux along the boundary of the bubble.

The flow solution is done under the assumption that $R(\theta)$ is a known function. In the next stage the shape is established by the evaluation of the normal stress. However the flow field is strongly dependent on the domain of the second phase. Hence shape and flow are solved iteratively till both are converged.

Implementation of such a solution scheme requires automatic grid generation. This is done by using transfinite interpolation scheme. The details of the interpolation scheme is described in Appendix-5. Grid generation using the transfinite interpolation requires that the coordinate of boundary of the domain be specified. For outside, i.e., for liquid phase, efficiency of the computation depends on $r = r_\infty$ be cut at a considerable distance from the bubble but without losing the accuracy. Therefore for outside, exponential distribution is adopted for elemental size. The advantages of such a distribution are

(1) The mesh is very fine in the more disturbed region, i.e., adjacent to the bubble surface.

(2) The number of elements does not increase to a large extent so that computational time is less without loss of accuracy.

However for inside the distribution is linear. Again for inside the first set of element emerge to be triangular. But two triangular elements are combined to form an isoparametric rectangular element. This is done just to avoid the complicity that would emerge for handling the triangular elements with rectangular elements adjacent to it. The disadvantages of adoption of such a method are

(1) The first set of elements that emerges from the center is fixed.

(2) Very large deformation of the bubble can not be considered.

The grid used is shown in Figure 3.2a and 3.2b. One important aspect of the grid generation technique is the distribution of the first point on both the axes. After the deformation one side gets compressed and other side is expanded. Hence for each iteration step this has to be adjusted so that the mesh be finest adjacent to the bubble surface.

The numerical calculations have been done using the above mentioned formulations for three different bubble diameter. The results obtained are presented in the next chapter.

CHAPTER IV

RESULTS AND DISCUSSIONS

Numerical solutions of the model discussed in chapter-II were obtained using typical values for the parameters of the problem. The physical properties were taken as constants for all the computational runs and their values are summarized in table 4.1. Results have been obtained for the shapes of the bubbles of different sizes, at different depths of the bath. The transient concentration profiles both inside and in the mass boundary layer have also been obtained. The variations of drag coefficient with Reynolds number and Eötvös number were also calculated with bubble rise. The results are presented and discussed below.

4. 1. Validation of the Model for shape calculation:

In fig. 4.1, the shape of a falling rain drop has been presented. Experimental data for the shape of bubbles in liquid metal bath were not available in literature. This because of the formidable difficulties associated with taking photographs in opaque and hot liquid metal medium. Therefore to check the accuracy and validity of the computational scheme used for the prediction of shape, the shape of a falling drop in air was predicted.. Figure 4.1b is the numerically predicted shape which matches to a very good accuracy with the experimental photograph of the rain drop of the same size, provided by Choji and Morogon [53Mac]. From the comparison, it is evident that the computational scheme we have used for the shape calculation is correct.

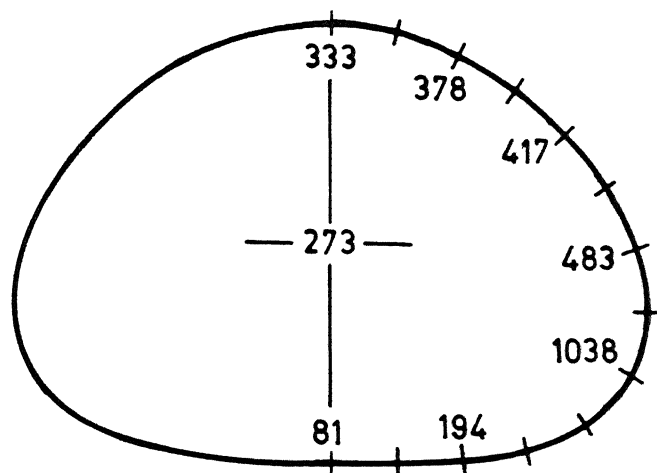


FIG. 4.1a. ACTUAL PHOTOGRAPH OF RAINDROP
(DIA. 6 mm) [PROVIDED BY CHOJI
MAGONO]

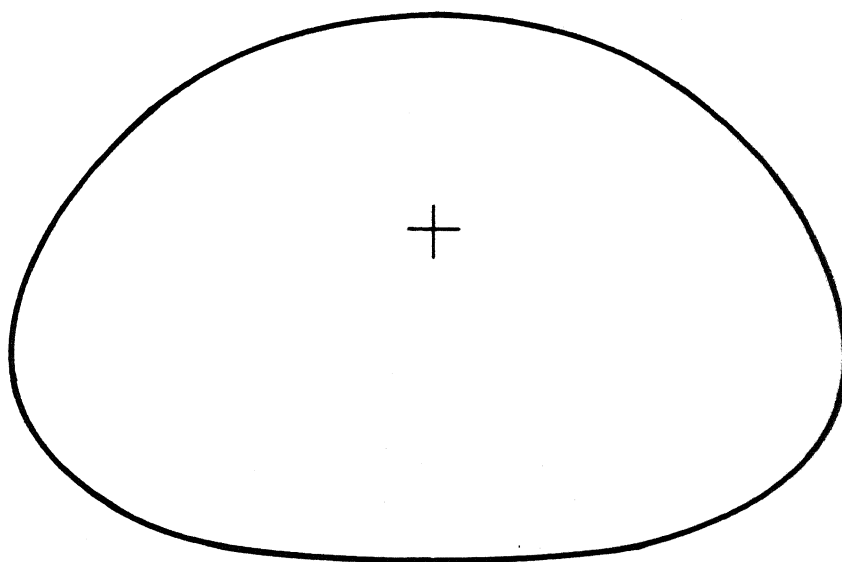


FIG. 4.1b. NUMERICALLY PREDICTED SHAPE OF
RAINDROP OF SAME SIZE .

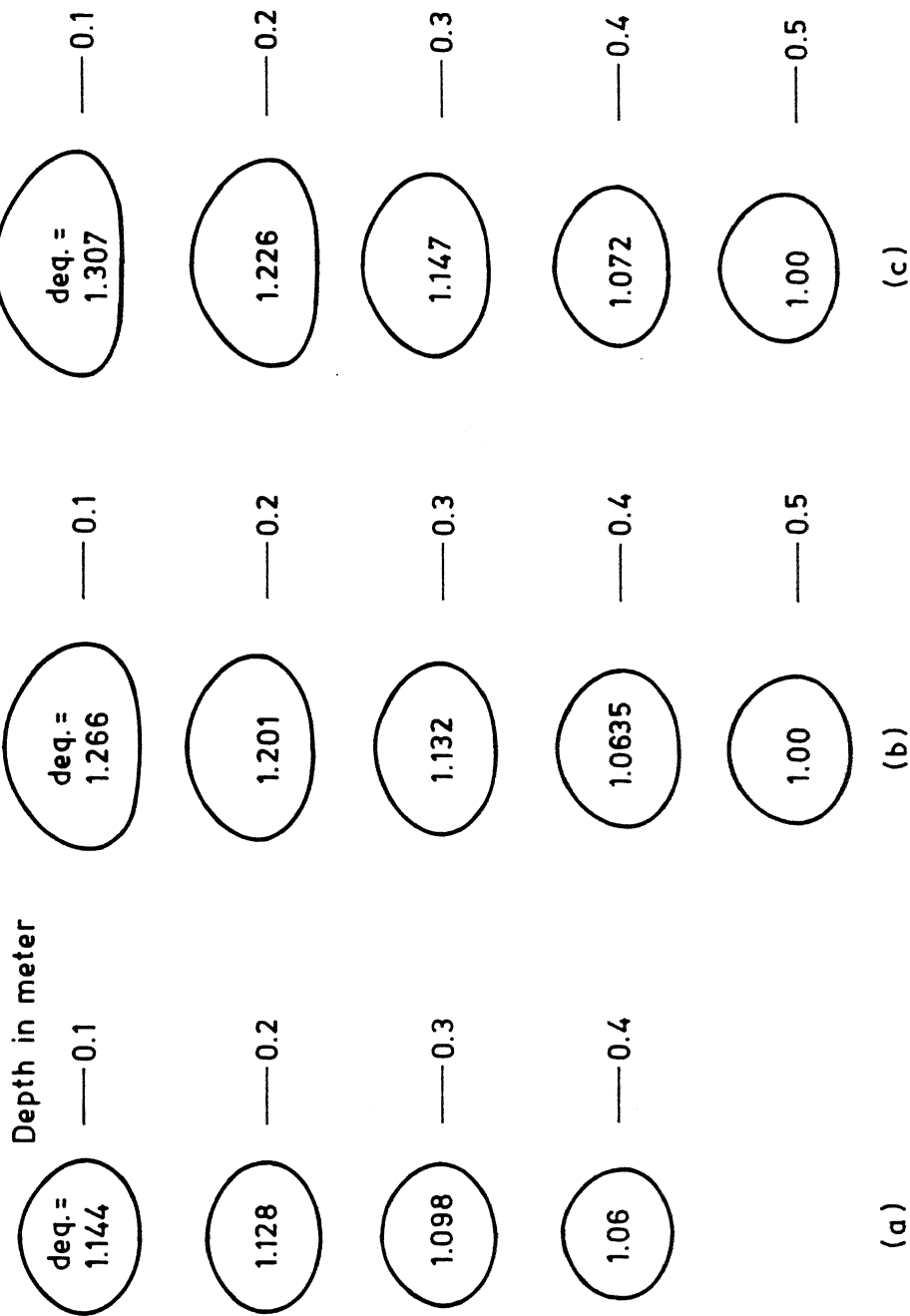


FIG. 4.2. SHAPE OF RISING BUBBLE AT DIFFERENT DEPTHS.
 (a) 2mm, (b) 4mm, (c) 5mm

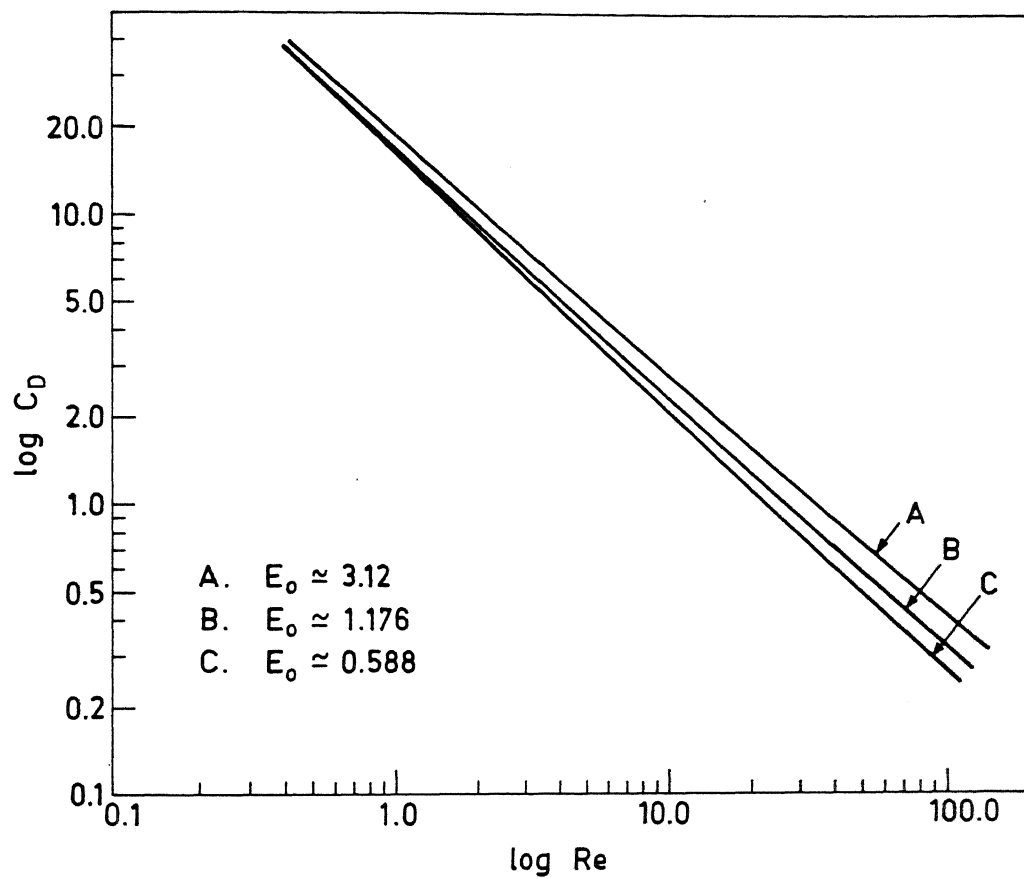


FIG. 4.3. DRAG COEFFICIENT vs. REYNOLDS NUMBER AT ONE HEIGHT AT DIFFERENT Eötvös NUMBER.

4.2 Results and discussions.

Figure 4.2a to c, present the shapes of rising bubbles in a liquid metal bath. From the figures it is clear that as the bubble size increases, the deformation becomes more. Since the static pressure decreases considerably with bubble rise, the volume of the bubble increases. Consequently the deformation becomes more severe. The bubble deforms from spherical to obloid ellipsoidal shape. When the bubble reaches the free surface the volume drastically changes. For this reason it has not been possible to predict the shape of the bubble very much near to the free surface. In general the bubble has flat bottom and a curved top surface. The flat bottom surface is believed to be a consequence of the dynamic pressure (in liquid) being very low in the wake behind the bubble. This explanation is corroborated by the streamline patterns discussed later. With respect to the initial value of equivalent bubble diameter (d_{eq}), it is seen that larger the value of d_{eq} , larger is the departure from spherical shape. This is not surprising as larger bubbles experience greater buoyancy and inertial effects. The increase in buoyancy is only due to size increase while that of inertia is both to the size and velocity change.

Figure 4.3 shows the variation of the drag coefficient with Reynolds number, for different Eötvös numbers. As the Reynolds number increases, the drag coefficient decreases. With respect to Eötvös number on the other hand C_D increases. The effect of Reynolds number on C_D is well known. For low Reynolds number C_D varies as $1/Re$ and the present study indicates that this variation is approximately true for bubble also in the range $0 \leq Re \leq 100$. The drag coefficient decreases with Re because of the weakening of viscous forces in comparison with inertia, at higher Re . The drag coefficient increases with $Eö$ because of the larger contribution from the form component of the drag force. The deformation becomes more at higher $Eö$ and hence the form drag

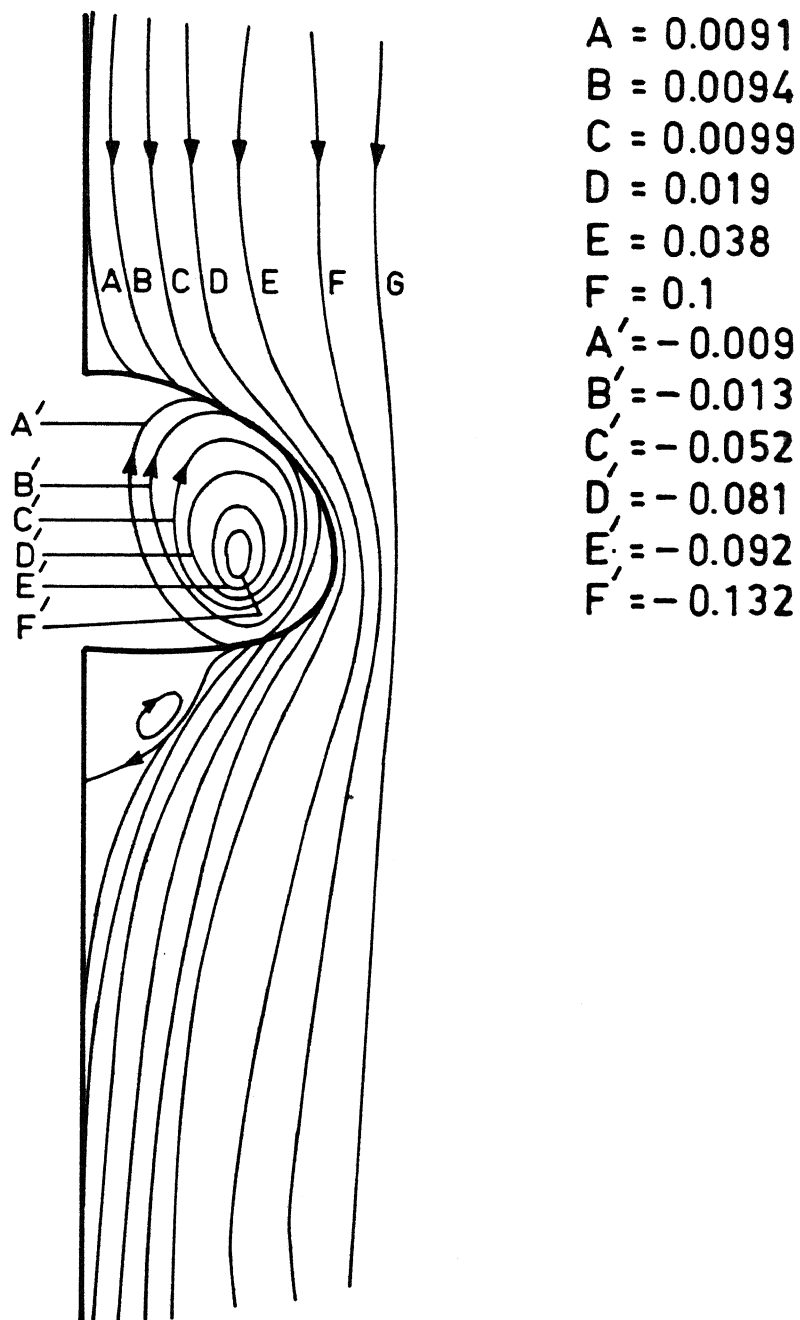


FIG. 4.4a. STREAMLINES AT
 $Re_{\text{outside}} = 100$, $Re_{\text{inside}} = 4.0$,
 Eötvös number = 3.12

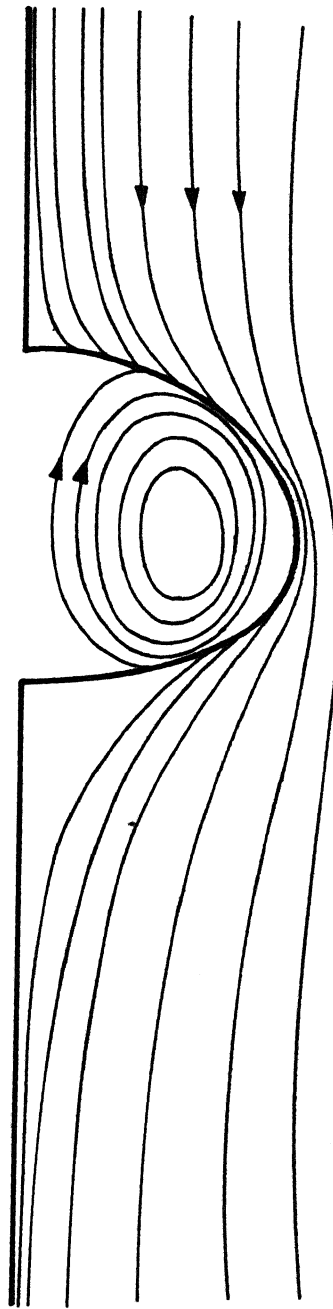


FIG. 4.4b. STREAMLINES AT
 $Re_{\text{outside}} = 50$, $Re_{\text{inside}} = 2.0$,
Eötvös number = 3.12

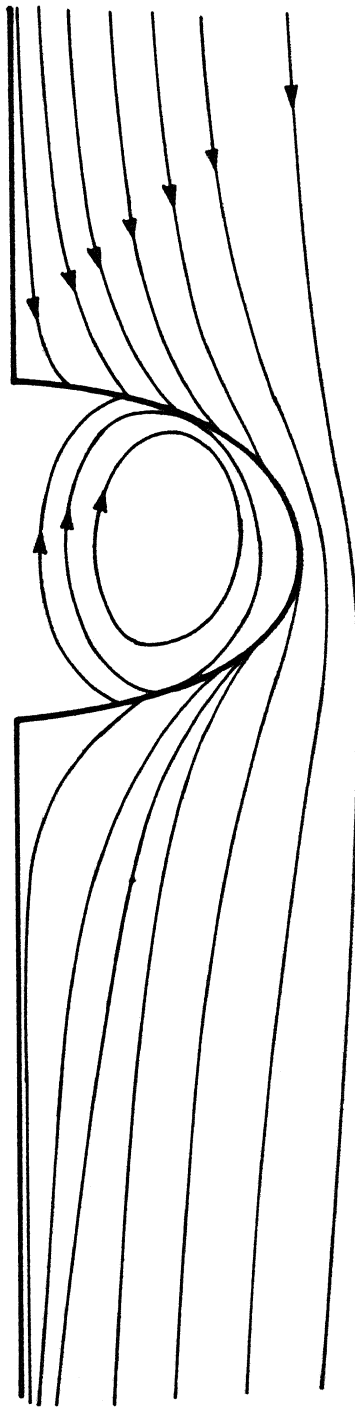


FIG. 4.4c. STREAMLINES AT
 $Re_{\text{outside}} = 20$, $Re_{\text{inside}} = 1.0$,
Eötvös number = 3.12

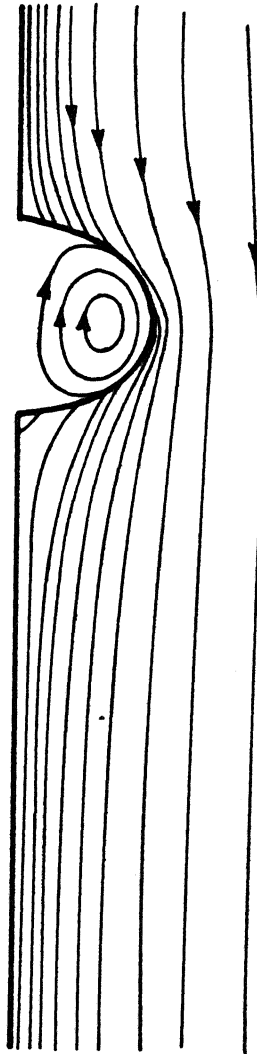


FIG. 4.4d. STREAMLINES AT
Re outside = 100, Re inside = 4.0,
Eötvös number = 1.176

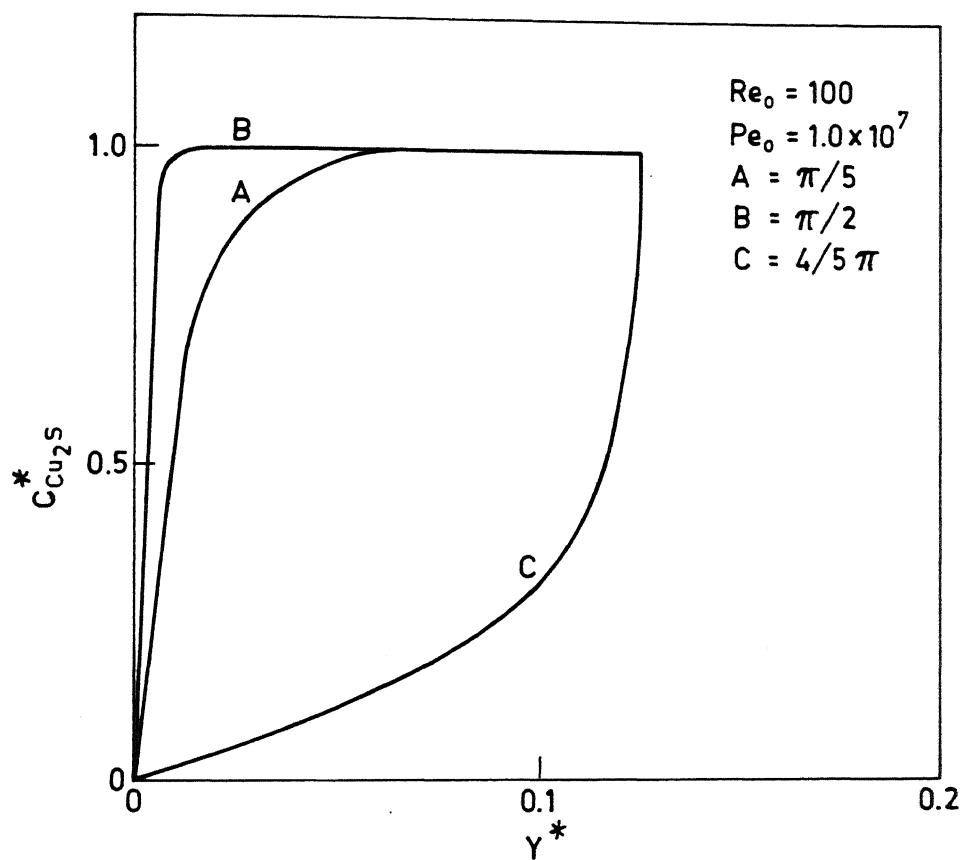


FIG. 4.5 DISTRIBUTION OF Cu_2S IN MASS TRANSFER BOUNDARY LAYER.

component increases.

Figure 4.4 a to d presents the stream lines both inside and outside the bubble for different Reynolds numbers. It is seen that the flow field and the shape are very sensitive to the Reynolds number. The inside flow pattern changes with shape to a large extent. However the vortex center is more or less located in the vicinity of 0.7 (non-dimensional radius), as for a potential flow vortex inside the bubble. At the external Reynolds numbers of 20 and 50, the circulation pattern inside the bubble exhibits fore and aft symmetry. At $Re_0 = 100$, the vortex moves closer to the front stagnation point, possibly due to maximum surface shear sources in the front region, at higher Re . This asymmetry may be due to the separation of external flow. As the external Reynolds number crosses about 50, the flow separates behind the bubble. At high $E8$, however, the critical Reynolds number for flow separation decreases due to larger bubble deformation. For solid spheres, it is known that flow separation occurs at a Reynolds number of around 20. For bubbles, this limit is higher because they offer no viscous tangential stress. Beyond Reynolds number 100 and $E8$ number about 3, the shape of the bubble becomes instable. For this reason it was not possible to predict the spherical cap bubbles which are generally encountered in metallic systems.

Figure 4.5 shows the variation of concentration of Cu_2S with angular positions within the mass transfer boundary layer. It is observed that there is a sharp boundary layer in the frontal regions of the bubble, whereas the boundary layer is very thick near the rear stagnation point. These findings are in conformity with those of Chao [69Cha].

Figure 4.5a shows the variation of oxygen concentration along $\theta = \pi/2$ at 0.04 nondimensional time for different gas phase mass peclet numbers. It is clear that the maximum concentration happens to be near the vortex center, this being a stagnation zone. Again with the increment of Re_i and Pe_i this zone becomes narrower and sharper. The profile indicates the existence of a

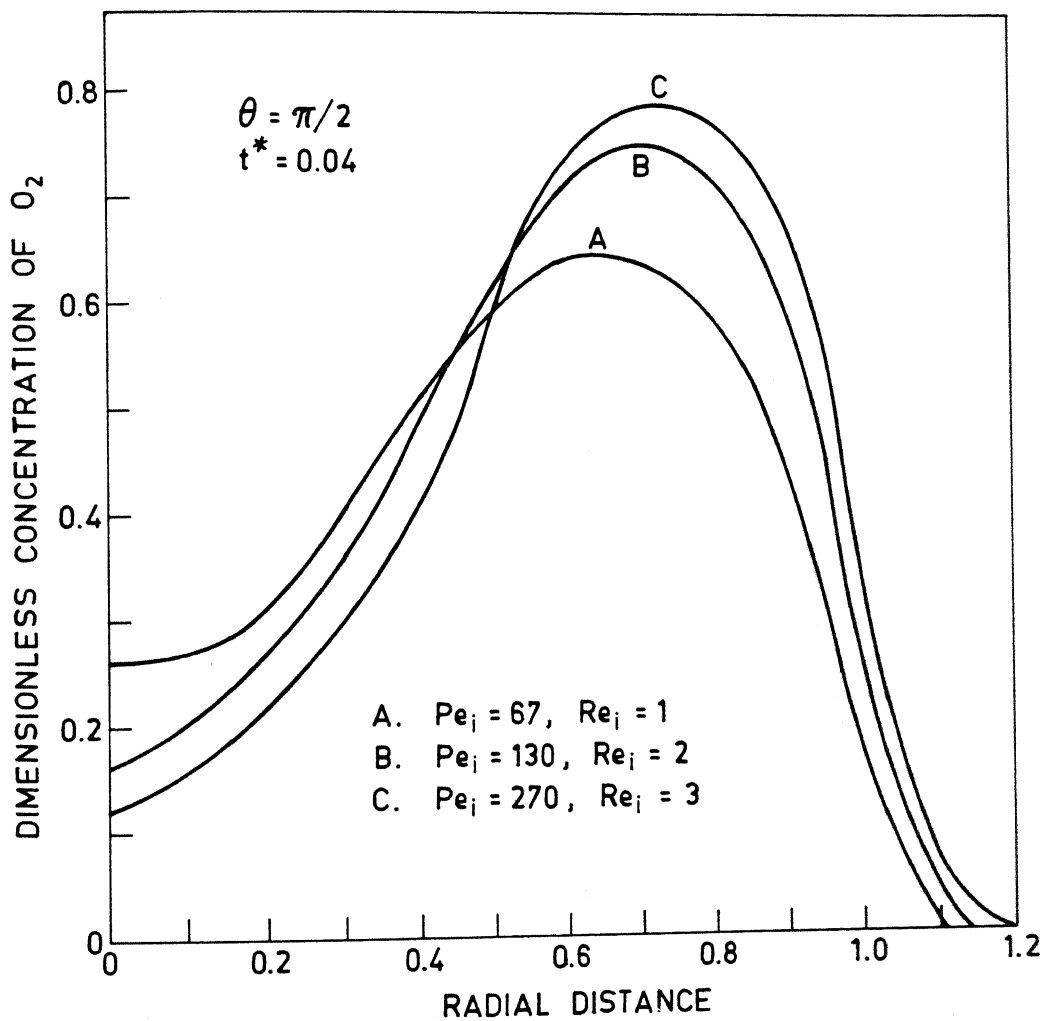


FIG. 4.5a. O_2 CONCENTRATION IN GAS PHASE AT $\theta = \pi/2$ ALONG RADIAL DISTANCE.

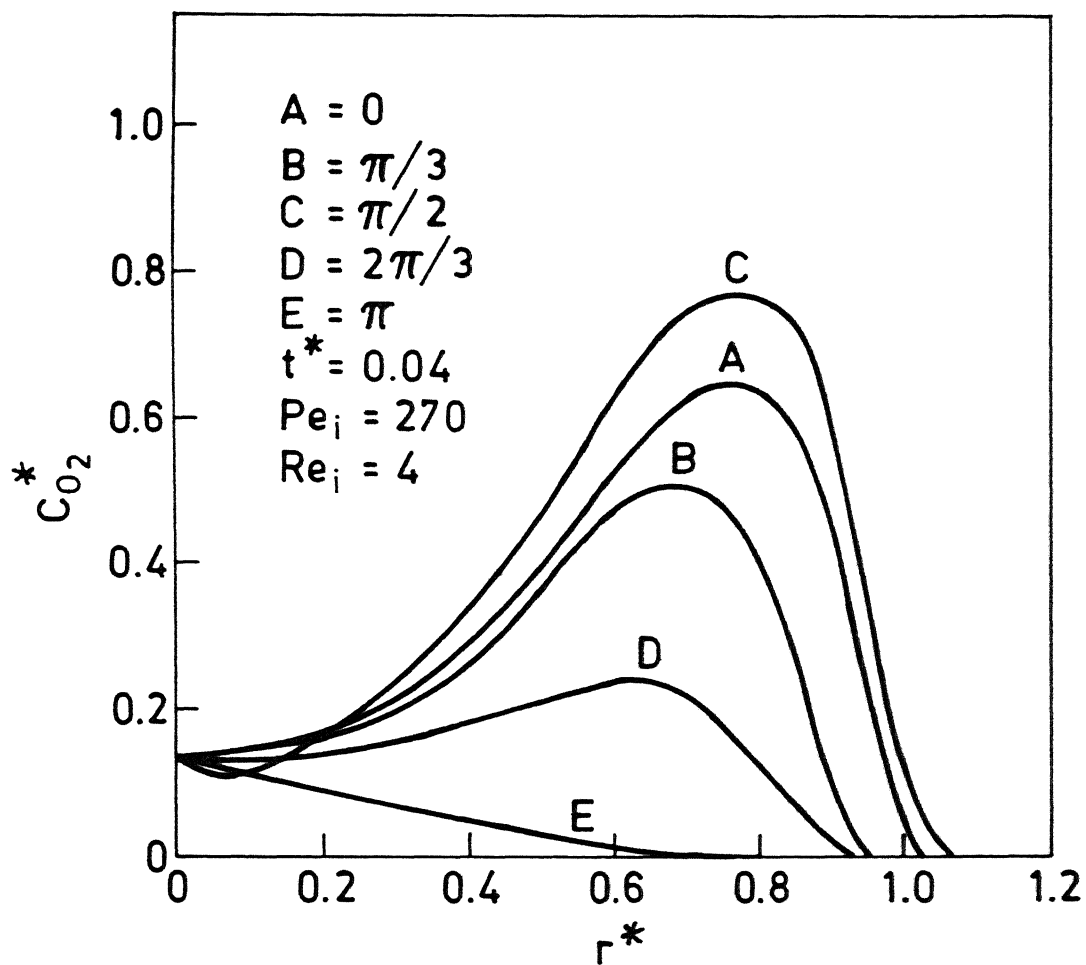


FIG. 4.5b. CONCENTRATION PROFILE AT DIFFERENT LOCATION AT FIXED TIME .

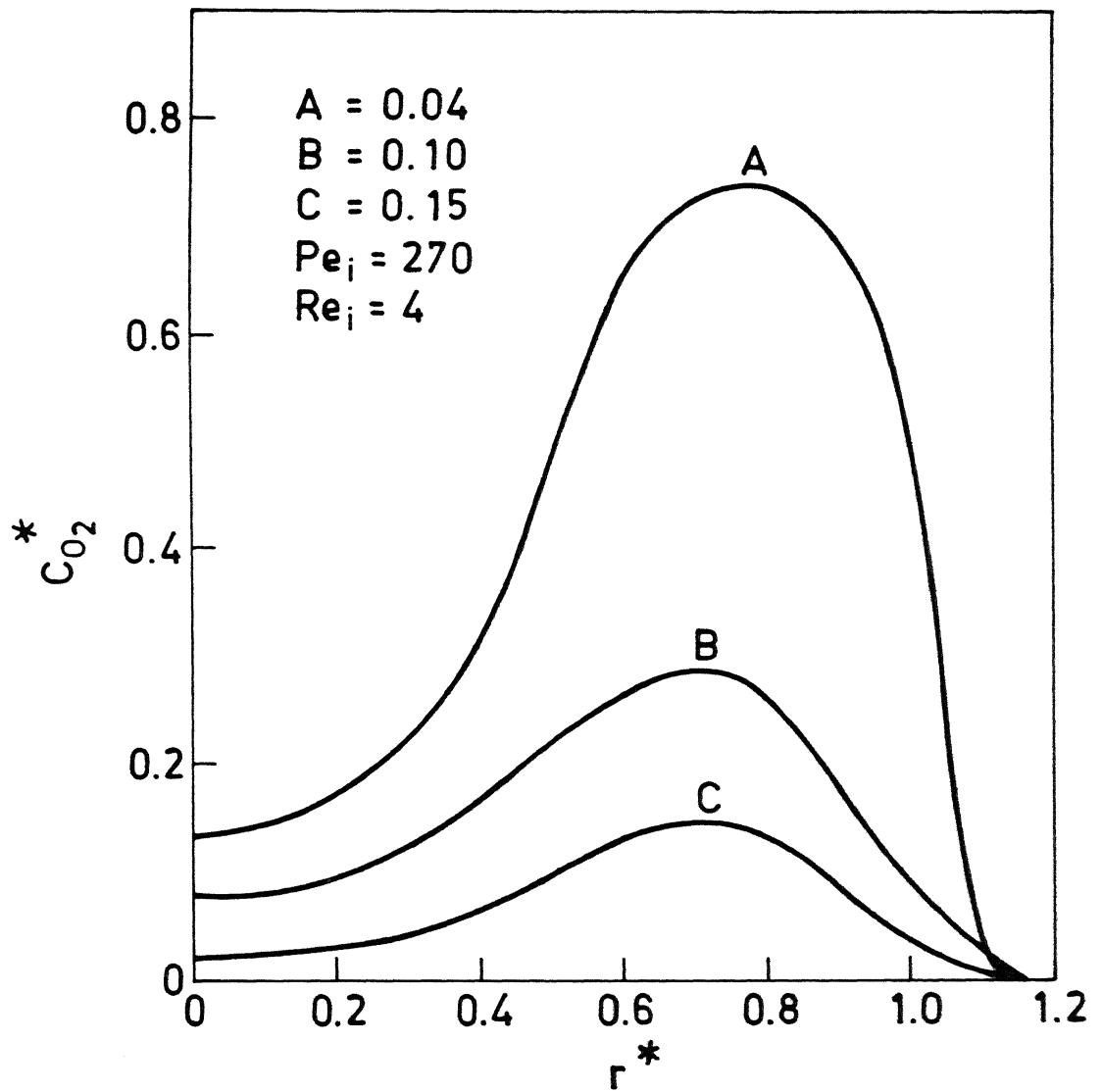


FIG. 4.5c. VARIATION OF CONCENTRATION PROFILE AT $\pi/2$ WITH TIME.

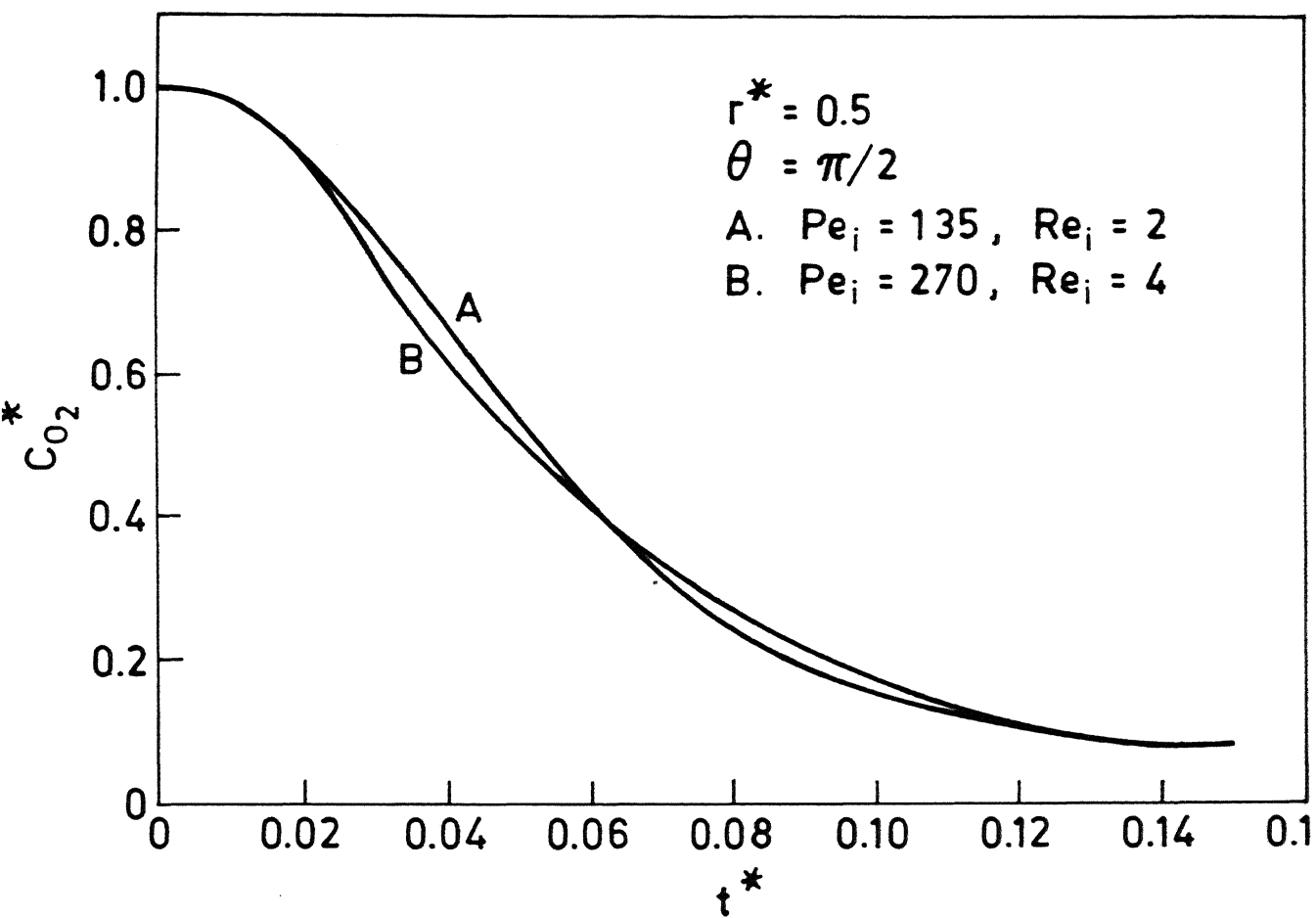


FIG. 4.5a VARIATION OF CONCENTRATION AT ONE POINT WITH TIME.

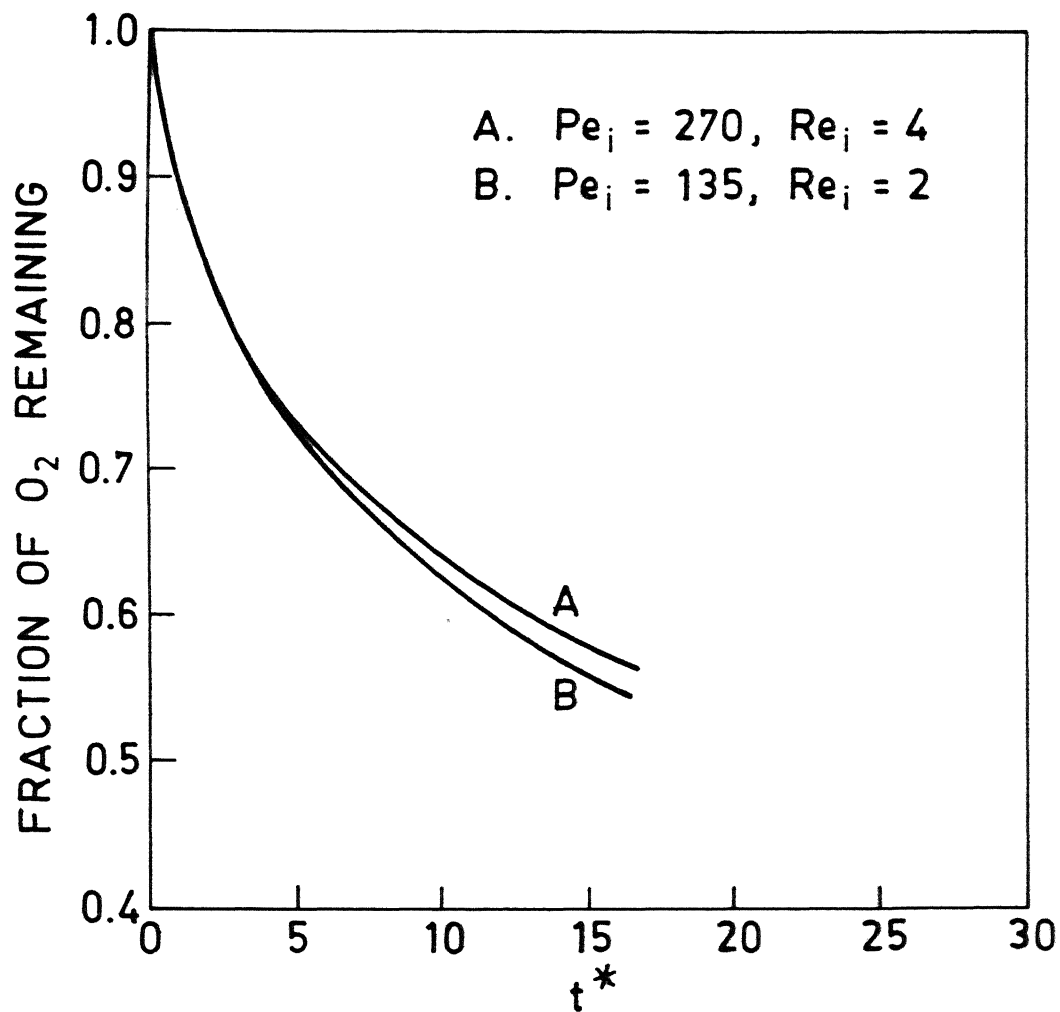


FIG. 4.5e. FRACTION OF O_2 LEFT IN GAS PHASE AT DIFFERENT TIME.

steep mass transfer boundary layer near the bubble surface, an oxygen deficient internal wake near the axis and an oxygen rich core. These features have been theoretically predicted and discussed in detail by Brignell [75Bril]. Figure 4.5b presents the variation of oxygen at different θ along the radial distance. It is observed that as θ nears the front stagnation point the region is depleted of oxygen. This is because of the strong circulation that is established inside the bubble. Thus the air that comes from the frontal region to the rear region is devoid of oxygen due to reaction at the interface. Figure 4.5c shows the depletion of oxygen with time, at $\theta = \pi/2$ along the radial distance. Here as time progresses the radial distance at $\theta = \pi/2$ increases due to deformation. However the concentration at the vortex center remain at maximum for all the time steps. Figure 4.5d presents the variation of O_2 at a point at different times. It is noticed that initially the concentration falls down rapidly but as time progresses the drop becomes slow. This is because initially depletion rate of oxygen is very high since the amount of oxygen available is high. But towards the end, the reaction slows down due to lack of oxygen inside the bubble. For lower inside mass peclet number the depletion of oxygen is faster because of higher rate mass transfer. The above mentioned ideas are reinforced in the figure 4.5e which shows the variation of available oxygen fraction within the bubble with time.

The transport, flow and shape change results predicted in the present work, thus are in conformity with the observations of earlier investigators. Elaborate comparison however, have not been possible due to the paucity of detailed results in the literature. The present study thus offers a powerful solution technique for solving the complex flow and transport processes in and around non-spherical bubbles.

CHAPTER-V

CONCLUSIONS AND SUGGESTION FOR FUTURE WORK

From the results obtained in the present study, the following conclusions can be drawn.

- The present model offers a powerful solution technique involving complex flow and transport processes in and around spherical bubbles for flows in low Reynolds number range ($0 \leq Re \leq 50$).

- The shape of the bubble, and flow, in and around are closely connected. The shape is sensitive to Reynolds number over a large extent in the range $0 \leq Re \leq 50$. Beyond this the variation is not large. For Re of the order of 200 the scheme fails to give a converged solution of the flow. These two aspects are so dependent on Eötvös number.

- The shape changes considerably near the free surface of the liquid. This is because of the sudden increment in the volume of the bubble.

- The basic nature of the transport is not significantly different from that of the spherical cases studied by earlier workers except in order of magnitude.

Conclusions:

The present study assumes that the flow is laminar. But in practical situations this may not be true. To simulate the practical situation it may be necessary to take the turbulent flow into account.

High Reynolds number should be tried. For this modified schemes e. g. upwind FEM schemes can be tried to obtain converged solution to the flow.

Here a single bubble behavior has been studied. Multi-bubble system can be studied to simulate practical situations.

A better interpolation technique can be developed which is not restricted to small deformations.

APPENDIX -I

MEAN CURVATURE OF A SURFACE OBTAINED BY REVOLVING A CURVE ABOUT AN AXIS :

Consider the surface obtained by revolving a curve in (X, Z) plane about Z -axis. Denoting by θ and ϕ the polar and azimuthal angles respectively, the equation for this surface in spherical co-ordinates is given by $r = R(\theta)$, where $R(\theta)$ is a function of θ . The mean curvature of a surface at a point P is defined as

$$K(P) = [K_n(\hat{n}_1) + K_n(\hat{n}_2)] \dots\dots\dots(1)$$

$K_n(\hat{n}_1)$ and $K_n(\hat{n}_2)$ are the normal curvatures along two mutually perpendicular directions \hat{n}_1 and \hat{n}_2 tangential to the surface at P . The normal curvature at a point on the surface along a direction \hat{n} , tangential to it at that point is given by

$$K_n(\hat{n}) = (\bar{\nabla}_n \bar{N}) \cdot \hat{n} \dots\dots\dots(2)$$

\bar{N} is the unit normal to the surface at the point and $\bar{\nabla}_n \bar{N} \cong$

$\sum_{i=1}^3 n_i \nabla_i \bar{N}$ is the rate at which the unit normal to the

surface turns as it is moved along the direction \hat{n} . It can be seen that the normal curvature $K_n(\hat{n})$ along a direction is the curvature of the curve on the surface obtained by its intersection with the plane containing \bar{N} and \hat{n} . It can also be shown that though only two mutually perpendicular directions \hat{n}_1 and \hat{n}_2 on the tangent plane are used to evaluate the mean curvature, the same value will be obtained when the mean is calculated over all directions tangential to the plane at the point. In this sense it may be said that the mean curvature for a surface is the mean value of the curvature of all normal curves (i. e. curves obtained by the intersection of the surface with the plane containing the normal to the surface) on the surface and passing through the given point. We now proceed to calculate the mean curvature at a point (θ, ϕ) on the surface, defined in eqn-1. At such a point the unit normal \bar{N} is given by

$$\bar{N} = \frac{\bar{\nabla} f(r, \theta, \phi)}{|\bar{\nabla} f|}$$

$f(r, \theta, \phi) = 0$ is the equation of surface. In the present case we have $f(r, \theta, \phi) = r - R(\theta)$, so that

$$\begin{aligned}\bar{N} &= (\hat{r} - R' \hat{\theta}) / (1 + R'^2/R^2)^{1/2} \\ &= (R \hat{r} - R' \hat{\theta}) / (R^2 + R'^2)^{1/2} \dots\dots\dots (3)\end{aligned}$$

$\bar{\nabla} = \hat{r} \partial/\partial r + \hat{\theta}/r \partial/\partial \theta + \hat{\phi}/r \sin \theta \partial/\partial \phi$ in the spherical coordinates, $\hat{r}, \hat{\theta}, \hat{\phi}$ are the unit vectors in the directions of increasing r, θ and ϕ respectively. In terms of the unit vector \hat{i} , along the three cartesian axes x, y and z , we have

$$\left. \begin{aligned}\hat{r} &= \sin \theta \cos \phi \hat{i} + \sin \theta \sin \phi \hat{j} + \cos \theta \hat{k} \\ \hat{\theta} &= \cos \theta \cos \phi \hat{i} + \cos \theta \sin \phi \hat{j} - \sin \theta \hat{k} \\ \hat{\phi} &= -\sin \phi \hat{i} + \cos \phi \hat{k}\end{aligned} \right\} \quad (4)$$

Mutually perpendicular unit vectors \hat{n}_1 and \hat{n}_2 in the plane can be chosen as:

$$\hat{n}_2 = \hat{\phi} \quad \text{and} \quad \hat{n}_1 = \hat{n}_2 \times \bar{N} = (R \hat{\theta} + R' \hat{r}) / (R^2 + R'^2)^{1/2} \dots\dots\dots (5)$$

For the calculation of the normal curvatures along \hat{n}_1 and \hat{n}_2 we need the vectors $\hat{n}_1 \cdot \bar{\nabla}$ and $\hat{n}_2 \cdot \bar{\nabla}$, which are easily obtained as

$$\hat{n}_1 \cdot \bar{\nabla} = 1/(R^2 + R'^2)^{1/2} [R' \partial/\partial r + \partial/\partial \theta] \dots\dots\dots (6)$$

$$\hat{n}_2 \cdot \bar{\nabla} = 1/R \sin \theta \partial/\partial \phi$$

It can be noted that in the above expressions for $\hat{n}_1 \cdot \bar{\nabla}$ and $\hat{n}_2 \cdot \bar{\nabla}$ we have put $r = R(\theta)$, corresponding to the interface. (3) and (6)

$$\begin{aligned}&= 1/(R^2 + R'^2)^{1/2} \partial/\partial \theta (R \hat{r} - R' \hat{\theta}) / (R^2 + R'^2)^{1/2} \\ &= 1/(R^2 + R'^2) \left[(R' \hat{r} + R \partial \hat{r} / \partial \theta - R'' \hat{\theta} - R' \partial \hat{\theta} / \partial \theta) / (R^2 + R'^2) \right. \\ &\quad \left. - (R \hat{r} - R' \hat{\theta})(R R' + R' R'') / (R^2 + R'^2)^{3/2} \right]\end{aligned}$$

in eqn (4) we have

$$\partial \hat{r}/\partial \theta = \hat{\theta} \quad \text{and} \quad \partial \hat{\theta}/\partial \theta = -\hat{r} \quad \text{so that}$$

$$\begin{aligned} \hat{\theta} \cdot \bar{\bar{N}} &= 1/(R^2 + R'^2) \left[2R'\hat{r} + (R - R'')\hat{\theta} - \frac{(R\hat{r} - R'\hat{\theta})(R\hat{r}' + R'R'')}{(R^2 + R'^2)} \right] \\ &= 1/(R^2 + R'^2)^2 \left[(R^2 + R'^2)(2R'\hat{r} + (R - R'')\hat{\theta}) - (R\hat{r}' + R'R'')(\dots R\hat{r} - R'\hat{\theta}) \right] \\ &= 1/(R^2 + R'^2)^2 \left[(R^2R' + 2R'^3 - R\hat{r}'R'')\hat{r} + (R^3 + 2R\hat{r}'R^3 - R^2R'')\hat{\theta} \right] \\ (\hat{n}_2 \cdot \hat{\theta}) \cdot \bar{\bar{N}} &= 1/R \sin \theta \cdot 1/(R^2 + R'^2)^{1/2} \left[R \partial \hat{r}/\partial \phi - R' \partial \hat{\theta}/\partial \phi \right] \quad \dots (7) \end{aligned}$$

Using $\partial \hat{r}/\partial \phi = \sin \theta \hat{\phi}$ and $\partial \hat{\theta}/\partial \phi = \cos \theta \hat{\phi}$ we obtain

$$\hat{\theta} \cdot \bar{\bar{N}} = 1/R \sin \theta \cdot 1/(R^2 + R'^2)^{1/2} \left[(R \sin \theta - R' \cos \theta) \hat{\phi} \right]$$

Similarly

$$\begin{aligned} (\hat{n}_1) &= \hat{n}_1 \cdot [(\hat{n}_1 \cdot \hat{\theta}) \cdot \bar{\bar{N}}] = 1/(R^2 + R'^2)^{5/2} \left[R^2 + R'^2 + 2R'^4 - R\hat{r}'R'' + R^4 + \dots + 2R^2R'^2 - R^3R'' \right] \\ &= 1/(R^2 + R'^2)^{5/2} \left[(R^2 + R'^2)^2 + R^2R'^2 + R'^4 - R\hat{r}'R'' - R^3R'' \right] \\ &= 1/(R^2 + R'^2)^{5/2} \left[(R^2 + R'^2)^2 + R'^2(R^2 + R'^2) - R\hat{r}''(R^2 + R'^2) \right] \\ &= 1/(R^2 + R'^2)^{5/2} \left[R^2 + 2R'^2 - R\hat{r}'' \right] \quad \dots \dots \dots (8) \end{aligned}$$

$$(\hat{n}_2) = \hat{n}_2 \cdot [(\hat{n}_2 \cdot \hat{\theta}) \cdot \bar{\bar{N}}] = \frac{R \sin \theta - R' \cos \theta}{R \sin \theta (R^2 + R'^2)^{1/2}}$$

It stands $K_n(\hat{n}_2)$ can either be positive or negative depending whether $R \sin \theta > R' \cos \theta$ or $R \sin \theta < R' \cos \theta$. However if $\bar{\bar{N}}$ is outward normal to the surface which is true of $\bar{\bar{N}}$ in eqn (3), $K_n(\hat{n}_2)$ is always +ve. Hence we take the modulus of the RHS considered in the expression for $K_n(\hat{n}_2)$. Thus,

$$\hat{n}_2 \cdot [(\hat{n}_2 \cdot \bar{\nabla}) \bar{N}] = \frac{|R \sin \theta - R' \cos \theta|}{R \sin \theta (R^2 + R'^2)^{1/2}} \dots\dots\dots (9)$$

in θ is always +ve for $0 \leq \theta \leq \pi$)

obtain

$$\frac{R^2 + 2R'R'' - R R'''}{(R^2 + R'^2)^{3/2}} + \left[\frac{|R' \cos \theta - R \sin \theta|}{R \sin \theta (R^2 + R'^2)^{1/2}} \right] \dots\dots\dots (10)$$

an curvature at a point on the surface obtained by the curve $r = R(\theta)$ on the X-Z plane about Z-axis.

APPENDIX- 2

COUPLING OF ENERGY EQUATION WITH MOMENTUM EQUATION :

Using Boussinesq approximation one can proceed with the assumption that the density varies in the buoyancy term of the momentum equation and every where else there is a average density $\bar{\rho}$.

Then pressure can be expressed as

$$P = P_{\text{static}} + P_{\text{dynamic}}$$

where static pressure is $P_{\text{static}} = P_0 + \bar{\rho} g z$

$\bar{\rho}$ is the average density of the fluid.

P_0 is atmospheric pressure

$$-\nabla p = (\bar{\rho} g - \rho g) \hat{k} - \nabla P_{\text{dynamic}}$$

$$= (\bar{\rho} - \rho) g \hat{k} - \nabla P_{\text{dynamic}}$$

Change in density $\Delta\rho$ can be expressed in terms of coefficient of thermal expansion as follows:

$$\beta = - \frac{1}{V} \frac{dV}{dT}$$

i. e., change in volume per unit volume per unit temperature difference)

$$\text{Where } V = \frac{1}{\rho}$$

$$\beta = \bar{\rho} \left(- \frac{1}{\bar{\rho}^2} \frac{\partial \bar{\rho}}{\partial T} \right) = - \frac{1}{\bar{\rho}} \frac{d\bar{\rho}}{dT}$$

$$\text{or } (\bar{\rho} - \rho) = \bar{\rho} \beta (T - \bar{T})$$

where \bar{T} is the reference temperature

$$\text{Then, } -\nabla p = \bar{\rho} g \beta (T - T_{\text{ref}}) \hat{k} - \nabla P_{\text{dynamic}}$$

In coupling momentum equation with the energy equation we have

$$\nabla \cdot \mathbf{V} = 0 \quad \dots\dots\dots (1)$$

$$\frac{\rho}{\tau} + \rho (\mathbf{V} \cdot \nabla \mathbf{V}) = \bar{\rho} g \beta (T - T_{\text{ref}}) \hat{k} - \nabla P_{\text{dynamic}} +$$

$$+ \nabla \cdot (\mu (\nabla \mathbf{V} + \nabla \mathbf{V}^T)) \quad \dots\dots\dots (2)$$

$$\frac{T}{t} + (\nabla \cdot \nabla T) = \alpha (\nabla^2 T) + S \quad \dots\dots\dots (3)$$

APPENDIX-III

CONDITION AT INFINITY OF OSEEN TYPE

One way of reducing the flow domain without losing accuracy to consider an Oseen type of flow at large r . As suggested by Oseen [85Chr] the flow at infinity can be thought of being generated from a point force applied to the origin of the coordinate system. The magnitude of this force is equal to the drag force exerted by the liquid on the bubble.

At sufficiently large distances from the bubble, the flow velocity differs slightly from the uniform profile U_∞ . The linearised Navier-Stokes equation regardless of the magnitude of Reynolds number is

$$U_\infty \left(\cos \theta \frac{\partial}{\partial r} + \frac{\sin \theta}{r} \frac{\partial}{\partial \theta} \right) \zeta = \nu \nabla^2 \zeta \quad (1)$$

Appropriate solution with the required symmetry is given by

$$\psi_2 = -2C_2 (\cos \theta + 1) [1 - \exp\{-rU_\infty (1 - \cos \theta)\}] \quad (2)$$

[64Van]

This solution gives a flow far from an arbitrary three dimensional body with no lifting force. In the present case this arises because the lifting force is absent owing to the symmetry of the flow. The constant C_2 depends only on certain details of the flow in the vicinity of the body, namely the drag force. The latter is supposed to be equal to the buoyancy force.

$$F_a = (\rho_l - \rho_g) gV$$

where ρ_g is the gas density which will be neglected as compared to the fluid density ρ_l . Also V denotes the volume of the bubble.

Now assuming that a sphere of radius b is situated at the origin of the coordinate system and b is selected so that the drag force exerted from the liquid on the bubble is equal to the drag force exerted on this imaginary rigid sphere, then

$$F_a = 6\pi\mu b U_\infty$$

$$\text{or, } b = \frac{gV}{6\pi\nu U_{\infty}} \quad (4)$$

It remains only to match the constant C_2 with this solution. For small r the stream function from (2) is represented as

$$\psi_2 = -2 C_2 (1+\cos \theta) r U_{\infty} / (2\nu) (1-\cos \theta) = -C_2 r U_{\infty} / \nu \sin^2 \theta \quad (5)$$

This solution has to be matched to Stoke's solution for a sphere of radius b , which is given by

$$\psi = -3/4 r b U_{\infty} \sin^2 \theta$$

From the above expression it is immediately seen that

$$C_2 = 3/4 \nu b$$

and thus

$$\psi = 1/2 U_{\infty} r^2 \sin^2 \theta - 3/2 \nu b (1+\cos \theta) [1-\exp\{-r U_{\infty} / \nu (1-\cos \theta)\}]$$

$$\text{From (4), } \psi = 1/2 U_{\infty} r^2 \sin^2 \theta - \frac{gV}{4\pi U_{\infty}} (1+\cos \theta) [1-\exp\{-r U_{\infty} / \nu (1-\cos \theta)\}] \quad (6)$$

The velocities can be determined from the definition of stream function at the cut off region and assigned as the boundary conditions.

APPENDIX-4

FRONTAL METHOD:

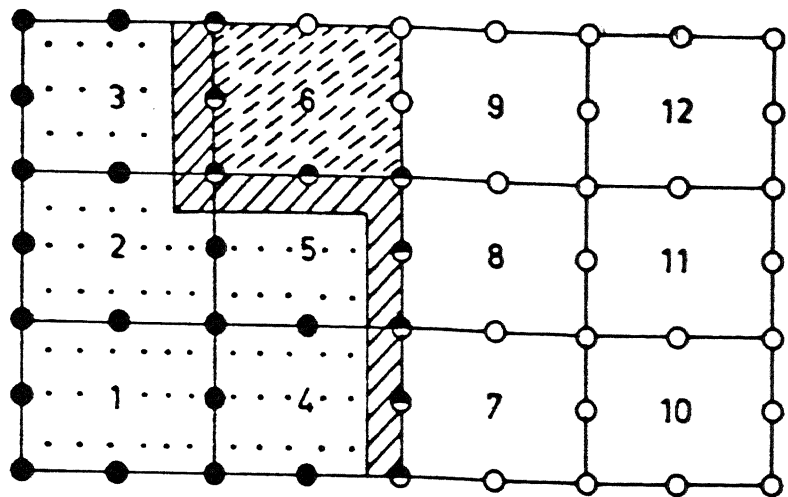
When the number of unknowns in the problem is very large, the method adopted for solving the assembled equations has significant bearing on the computer storage requirement and execution time. It would be uneconomical to solve these equations by simple matrix inversion techniques. The Frontal method is based on direct gaussian elimination method for solving symmetric matrices where the leading diagonal is always used as pivot. For unsymmetric matrices, encountered in a wide range of engineering problems, the most suitable pivot is not necessarily on the leading diagonal; and frontal solution routine exists for off diagonal pivoting [81Tay]. This, however, tends to be more time consuming. The method incorporated here uses only diagonal pivoting, but includes many features of the frontal technique for solving unsymmetric matrices.

In general terms, the overall solution technique consists of

- (1) Formation of Elemental Matrices.
- (2) Assembling into a global matrix.
- (3) Introduction of boundary conditions.
- (4) Reduction of global matrix using Gaussian elimination technique.
- (5) A back substitution process.

BASIC PHILOSOPHY OF THE FRONTAL METHOD :

The primary objective of the frontal method is the elimination of variables as soon as possible after their introduction into the global matrix via the appropriate equations. When the contributions from all the elements to a particular nodal point have been assembled, the corresponding variables associated with that node can be eliminated. The complete matrix is therefore never assembled since the reduced equation can be eliminated from the core and stored in the disc. The equations held in core and the corresponding nodes and variables are collectively called as front and the number of unknown variables in the front is termed as front width. The front width changes continually since only





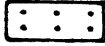
- Inactive Nodes
- Active Nodes
- ⊙ Deactivated Nodes
-  Front
-  Next Element for Assembly
-  Assembled Element

Fig. A4. Definition of Front and Element Number for Minimum Front Width.

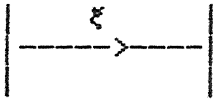
after the contribution to a particular node have been fully summed, the corresponding equation reduction based on a diagonal pivot can be executed.

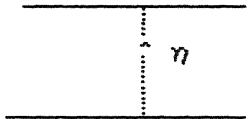
A pre assigned global matrix core area is first filled from contributing elements and the largest diagonal entry in the pre assigned core is found and used as pivot in a direct gaussian elimination process. As the maximum predetermined number of equations are eliminated, the corresponding reduced equations are written on to the disc and more elements and corresponding equations are taken into the core. Fig-A4 shows the basic idea of the frontal method. The equations, nodes, and variables currently in the core are termed "active"; those assigned to the disc are "deactivated"; and those yet to appear in core are "inactive" [73Tay].

APPENDIX - 5

TRANSFINITE INTERPOLATION:

In two dimensions a linear Lagrange interpolation function can be written in terms of interpolations in each curvilinear direction as:

$$\underline{r}(\xi, \eta) = \sum_{n=1}^2 \phi_n\left(\frac{\xi}{I}\right) \underline{r}(\xi_n, \eta) \dots\dots\dots(1)$$


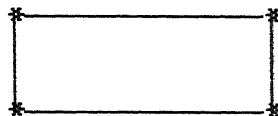
$$\underline{r}(\xi, \eta) = \sum_{m=1}^2 \psi_m\left(\frac{\eta}{J}\right) \underline{r}(\xi, \eta_m) \dots\dots\dots(2)$$


This interpolation is called transfinite since it matches the function on the entire boundary defined by $\xi = 0$ and $\xi = I$ in the first equation or by $\eta = 0$ and $\eta = J$ in the second.

The tensor product form is

$$\underline{r}(\xi, \eta) = \sum_{n=1}^2 \sum_{m=1}^2 \phi_n\left(\frac{\xi}{I}\right) \psi_m\left(\frac{\eta}{J}\right) \underline{r}_{nm} \dots\dots\dots(3)$$

where $\underline{r}_{nm} = \underline{r}(\xi_n, \eta_m)$ matches the function at the four corners



The sum of eqn(1) and eqn(2) is

$$\underline{S}(\xi, \eta) = \sum_{n=1}^2 \phi_n\left(\frac{\xi}{I}\right) \underline{r}(\xi_n, \eta) + \sum_{m=1}^2 \psi_m\left(\frac{\eta}{J}\right) \underline{r}(\xi, \eta_m) \dots\dots\dots(4)$$

Equation (4), when evaluated on $\xi = 0$ boundary gives

$$\underline{S}(0, \eta) = \underline{r}(0, \eta) + \sum_{m=1}^2 \psi_m\left(\frac{\eta}{J}\right) \underline{r}(0, \eta_m) \dots\dots\dots(5)$$

This does not match the function on the $\xi = 0$ boundary because of the second term in the right, which is an interpolation between the ends of this boundary

$$\underline{r}(0, J)$$

$$\bar{r}^*(0, \eta) \rightarrow \frac{\bar{r}^*(0, 1)}{\sum_{m=1}^2 \psi_m(-\frac{\eta}{J})} \bar{r}(0, \eta_m)$$

Similar effects occur on the other boundaries and the discrepancy on $\xi = 1$ boundary is

$$\sum_{m=1}^2 \psi_m(-\frac{\eta}{J}) \bar{r}(1, \eta_m)$$

The discrepancies on both these boundaries can be removed by subtracting from $\bar{S}(\xi, \eta)$, a function formed by interpolating the discrepancies between the two boundaries.

$$\bar{R}(\xi, \eta) = \sum_{n=1}^2 \phi_n(\frac{\xi}{I}) \left[\sum_{m=1}^2 \psi_m(-\frac{\eta}{J}) \bar{r}(\xi_n, \eta_m) \right] \dots \dots \dots (6)$$

This is simply the tensor product form given by eqn (3) which matches the function at the four corners.

The function $\bar{S} - \bar{R}$ then matches the function on all four sides of the boundary, so that we have the transfinite interpolation form,

$$\begin{aligned} \bar{r}(\xi, \eta) = & \sum_{n=1}^2 \phi_n(\frac{\xi}{I}) \bar{r}(\xi_n, \eta) + \sum_{m=1}^2 \psi_m(-\frac{\eta}{J}) \bar{r}(\xi, \eta_m) \\ & - \sum_{n=1}^2 \sum_{m=1}^2 \phi_n(\frac{\xi}{I}) \psi_m(-\frac{\eta}{J}) \bar{r}(\xi_n, \eta_m) \dots \dots (7) \end{aligned}$$

which matches the function on entire boundary.

The tensor product form

$$\bar{r}(\xi, \eta) = \sum_{n=1}^2 \sum_{m=1}^2 \phi_n(\frac{\xi}{I}) \psi_m(-\frac{\eta}{J}) \bar{r}(\xi_n, \eta_m) \dots \dots (8)$$

matches the function at the four corners of the boundary. This generalises to the interpolation from a set of $N+M$ intersecting curves for which the univariate interpolation is given by

$$\bar{r}(\xi, \eta) = \sum_{n=1}^N \phi_n(-\frac{\xi}{I}) \bar{r}(\xi_n, \eta) \quad (9)$$

M

$$r_{\underline{m}}(\xi, \eta) = \sum_1^M \psi_m \left(\frac{\eta}{J} \right) r_{\underline{m}}(\xi, \eta_m) \quad (10)$$

where now the blending functions, ϕ_n and ψ_m are any functions which satisfy the cardinality conditions

$$\phi_n \left(\frac{\xi}{I} \right) = \delta_{n1} \quad n=1, 2, \dots, N \quad 1=1, 2, \dots, N$$

$$\psi_m \left(\frac{\eta}{J} \right) = \delta_{m1} \quad m=1, 2, \dots, M \quad 1=1, 2, \dots, M \quad (11)$$

The general form of the transfinite interpolation then is

$$r_{\underline{m}}(\xi, \eta) = \sum_1^N \phi_n \left(\frac{\xi}{I} \right) r_{\underline{m}}(\xi_n, \eta) + \sum_1^M \psi_m \left(\frac{\eta}{J} \right) r_{\underline{m}}(\xi, \eta_m) - \sum_{n=1}^N \sum_{m=1}^M \phi_n \left(\frac{\xi}{I} \right) \psi_m \left(\frac{\eta}{J} \right) r_{\underline{m}}(\xi_n, \eta_m) \quad (12)$$

$$\text{or, } r_{\underline{m}}(\xi, \eta) = \sum_1^M \psi_m \left(\frac{\eta}{J} \right) r_{\underline{m}}(\xi, \eta_m) + \sum_{n=1}^N \phi_n \left(\frac{\xi}{I} \right) \left[r_{\underline{m}}(\xi_n, \eta) - \sum_{m=1}^M \psi_m \left(\frac{\eta}{J} \right) r_{\underline{m}}(\xi_n, \eta_m) \right]$$

The first term is the result at each point in the field of the unidirectional interpolation in the η direction and the bracket is the result of the difference between the specified values on the $\xi = \xi_n$ lines and result of the unidirectional interpolation on those lines. The two directional transfinite interpolations can thus be implemented in one direction, say η , over the entire field. Calling the result

$$F_{\underline{1}}(\xi, \eta) = \sum_1^M \psi_m \left(\frac{\eta}{J} \right) r_{\underline{m}}(\xi, \eta_m) \quad (13)$$

and interpolating the discrepancy on the $\xi = \xi_n$ lines over the entire field in the other direction, with the definition

$$F_{\underline{2}}(\xi, \eta) = \sum_1^N \phi_n \left(\frac{\xi}{I} \right) [r_{\underline{m}}(\xi_n, \eta) - F_{\underline{1}}(\xi_n, \eta)] \quad (14)$$

we get

$$r_{\underline{m}}(\xi, \eta) = F_{\underline{1}}(\xi, \eta) + F_{\underline{2}}(\xi, \eta) \quad (15)$$

This transfinite interpolation form is the best algebraically approximated [85Tho].

REFERENCES

- [54McD] McDonald, James E., Feb "The Shape of Rain Drops", The Physics of Everyday Phenomena, Scientific American, W. H. Freeman & Company, pp 23-27.
- [68Cox] Cox R. G., "The Deformation of a Drop in a General Time Dependent Flow", J. Fluid Mech., vol 37, Part-3, pp 601-623.
- [69Cha] Chao, B.T., J1. of Heat Transfer 91, pp273-281.
- [69Par] Parlange Jeans-Yves, "Spherical Cap Bubbles with Laminar Wakes", J of Fluid Mech., vol 37, Part-2, pp 257-268.
- [71Pru] Pruppacher, H. R. and Pitter R. L., "A semi Empirical Determination of the Shape of Cloud and Rain Drops", J Atmospheric Science, vol 28, pp 86-94.
- [73Bar] Barthes -Biesel and Acrivos A., "Deformation and Burst of a Liquid Droplet Freely Suspended in a Linear Shear Field", J Fluid Mech., vol 61, part-1, pp 1-21.
- [73Gra] Grace J. R. "Shapes Velocities of Bubbles Rising in Infinite Liquids", Trans. Instn. Chem. Engrs, vol 51, pp 116-120.
- [73Tay] Taylor, C. and Hood, P., "A Numerical Solution of the Navier-Stokes Equations Using Finite Element Technique", Computers and Fluids, Vol.-1, pp-73.
- [75Mur] Murr Lawrence, E. "Inter facial Phenomena in Metals and Alloys", Addison-Wesley Publishing Company, Inc., Massachusetts.
- [75Osl] Oslon, M. D., "Variational Finite Element Methods for Two-dimensional and Axisymmetric Navier-Stokes Equations", Finite Element in Fluids, Vol-1, Viscous Flow and Hydrodynamics, (Ed.) Gallagher, R. H., et al., John Willey, London.
- [75Bri] Brignel, A. S., Int. J1. of Heat and Mass Transfer, Vol. 18, pp 61-68, Jan.
- [76You] Youngren, G. K. and Acrivos A. "On the Shape of a gas Bubble in a Viscous Extensional Flow", J Fluid Mech., vol 73, part-3, pp 433-442.
- [76Bis] Biswas, A. K., Davenport, W. G., "Extractive Metallurgy of Copper", 2nd Edition, N. Y.
- [77Zie] Zienkiewicz, O. C., "The Finite Element Method in Engineering Science", McGraw Hill.
- [78Cli] Clift, R. , Grace, J.R. and Weber, M.E. "Bubbles, Drops and Particles", Academic Press, New York.

[78Hen] Henrich, J. C., Marshall, R. S. and Zienkiewicz, O. C., "Penalty Function Solution of Coupled Convective and Conductive Heat Transfer", Proc. Int. Conf. on Numerical methods in Laminar and Turbulent Flow, Swansea.

[79Sze] Szekely, J., "Fluid Flow Phenomena in Metal Processing", Academic Press, New York.

[81Tay] Taylor, C. and Hughes, T. G., "Finite Element Programming Of the Navier-Stokes Equations", Pineridge Press, Ltd., Swansea.

[81Bha] Bhaga, D. and Weber, M. E. "Bubbles in Viscous Liquids:- Shapes, Wakes and Velocities", J Fluid Mech., vol 105, pp 61-85.

[81Mik] Miksis J. Michael. "Shape of a Drop in an electric Field" Phys. Fluids, vol 24(11), pp 1967-1970.

[81Mik] Miksis, J. Michael. "A Bubble in an Axially Symmetric Shear Flow", Phys. Fluids, vol 24(7), pp 1229-1231.

[81Van] Vanden-Broeck, Jean-Marc. "Two Dimensional Drops in Slow Viscous Flow", Phys. Fluids, vol 24(1), pp 175-176.

[81Mik] Miksis Michael., Vanden-Broeck, Jean-Marc and Keller, Joseph B. "Axisymmetric Bubbles or Drops in a Uniform Flow" J Fluid Mech., vol 108, pp 89-100.

[81Ral] Rallison, J. M. "A Numerical Study of the Deformation and Burst of Viscous Drops in General Shear Flow" J Fluid Mech. vol 109, pp 465-482.

[82Mik] Miksis Michael, J. and Vanden-Broeck, Jean-Marc. and Keller Joseph, D. "Rising Bubbles" J Fluid Mech. pp 31-41.

[84Rys] Ryskin, G. and Leal, L. G. "Numerical Solution of Free Boundary Problem in Fluid Mechanics" Part-2, "Buoyancy-Driven Motion of Gas Bubbles Through a Quiescent Liquid" J Fluid Mech, vol 148, pp 19-35.

[84Rys] Ryskin, G. and Leal L. G. "A Numerical Solution of Free Boundary Problem in Fluid Mechanics", Part-1, Finite Difference Technique, J of Fluid Mech, vol 148, pp 1-17.

[84Har] Harper, J. F. "The Motion of Bubbles and Drops Through Liquids", Surveys in Applied Mechanics, pp 59-129.

[85Tho] Thompson, F. J., Warsi, Z. U. A., Martin, Wayne, C., "NUMerical Grid Generation", Elsevier Science Publishing Co. Inc., pp 310.

[88Das] Das, A., M. Tech. Thesis, I. I. T. Kanpur.